

# Dynamic evolution of competing same-dip double subduction: New perspectives of the Neo-Tethyan plate tectonics

Arnab Roy<sup>1</sup>, Nibir Mandal<sup>1</sup>, Jeroen Van Hunen<sup>2</sup>

<sup>1</sup>High Pressure and Temperature Laboratory, Department of Geological Sciences,  
Jadavpur University, Kolkata 700032, India.

<sup>2</sup>Department of Earth Sciences, Durham University, Durham, UK

## Abstract

*Same-dip double-subduction* (SDDS) systems are widely reported from present as well as past complex convergent plate tectonic configurations. However, the dynamics of their evolution is poorly understood, which is crucial to conceptualize anomalous subducting slab kinematics and associated observed geological phenomena, such as irregular trench migration rates, high convergence velocities, and slab break-off. To bridge this gap, we develop dynamic thermo-mechanical subduction models and investigate the initiation and evolution of SDDS systems, considering three different initial plate configurations: oceanic, oceanic-continental and multiple continental settings, based on Neo-Tethyan paleo-reconstructions. Each model offers new insights into the complex tectonic history of the major Neo-Tethyan subduction zones, particularly the Indo-Eurasian and Andaman convergent systems. We evaluate the slab-slab interactions, trench and subduction kinematics, inter-plate reorganization, and temporally varying mantle flow patterns involved in the dynamic evolution of these SDDS systems. The oceanic SDDS model simulations reveal that a sizable oceanic plate can initiate two subduction zones synchronously, and they evolve unequally in a competing mode, leading to exceptionally high convergence rates (~16-17 cm/year) for a prolonged duration (~7-8 Myr). This finding explains the coeval activity of coupled subduction zones in the Indo-Eurasia convergence during the Cretaceous evolution of the Neo-Tethys. We further implement a corresponding single subduction model to assess the additional effects of competing slab kinematics in an oceanic SDDS setting. The ocean-continent SDDS model, on the other hand, localizes subduction preferentially at passive margins between the oceanic plate and the continental block, forming double subduction zones that grow almost equally to form a spreading centre between the two trenches. These model results allow to reconstruct the Cenozoic evolution of the eastern Neo-Tethyan region, which ultimately led to the development of the Andaman subduction zone. We also show the post-Cretaceous evolution of the Indo-Eurasian collision zone as a consequence of the SDDS dynamics in presence of multiple continental blocks. These dynamics facilitated slab break-off, transforming the SDDS into a single subduction system in a relatively short time frame (~3 Myr). We finish with a synthesis of the paleo-reconstructions of the Neo-Tethys in the perspective of these SDDS models.

---

**Keywords:** Convergent plate tectonics, double subduction systems, dynamic subduction modelling, Finite element method, slab interaction, spreading centre locations, tectonic evolution of Neo-Tethys

1  
2  
3  
4  
5  
6  
7  
8  
9  
10  
11  
12  
13  
14  
15  
16  
17  
18  
19  
20  
21  
22  
23  
24  
25  
26  
27  
28  
29  
30  
31  
32  
33  
34  
35  
36  
37  
38  
39  
40  
41  
42  
43  
44  
45  
46  
47  
48  
49  
50  
51  
52  
53  
54  
55  
56  
57  
58  
59  
60  
61  
62  
63  
64  
65

# 32 1. Introduction

33 Subduction zones are spectacular planetary-scale manifestations of the convergent plate  
34 tectonics, and govern a wide range of geological phenomena, such as continental crust formation,  
35 magmatism and geochemical recycling, and geophysical processes, such as earthquake  
36 localization and energy dissipation (Corbi et al., 2017; Stern, 2002; Tilling, 1996). Subduction  
37 tectonics often turn complicated due to complex configurations of multiple plates, kinematically  
38 linked with one another. Double subduction systems are a common example of such convergent  
39 settings, where two lithospheric slabs subduct synchronously along sub-parallel trenches (Fig. 1).  
40 They are widely reported from the present-day plate configurations (Fig. 1), e.g., the  
41 Mediterranean (Király et al., 2018; Vignaroli et al., 2008), the Molucca Sea (Zhang et al., 2017),  
42 Taiwan (Lin and Kuo, 2016), New Zealand (Lamb, 2015), and around the Philippines plate

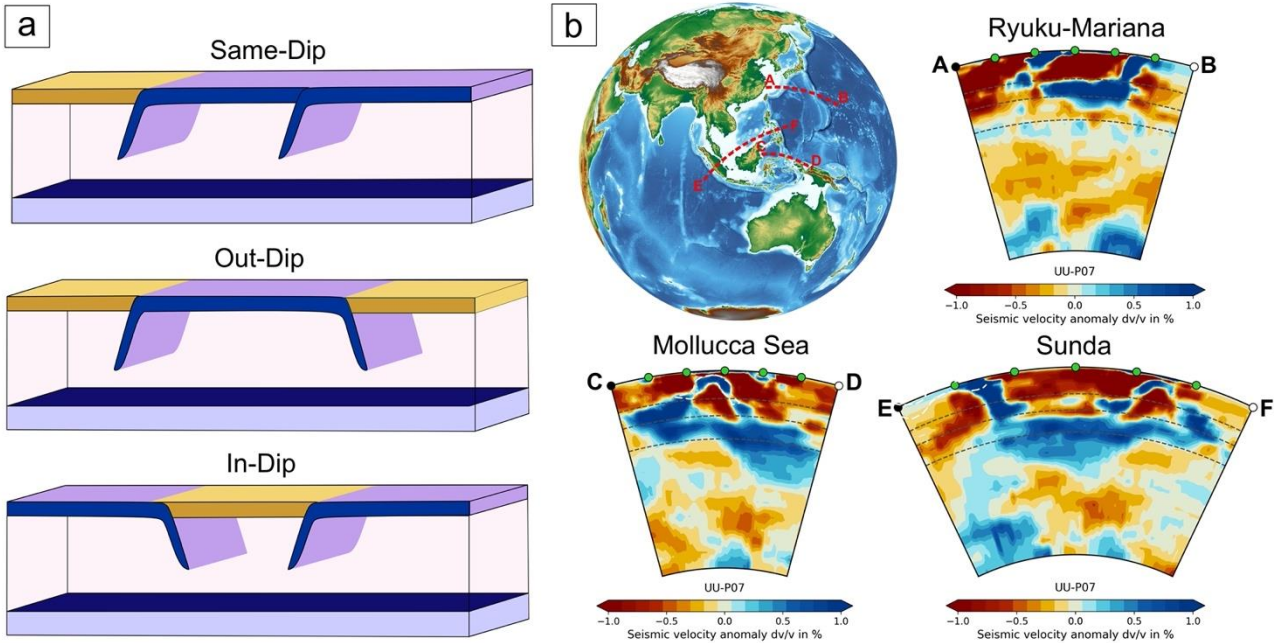


Figure 1: Illustrations showing a) the three different types of double subduction systems and b) their natural counterparts observed from seismic tomography. The P-wave model used for this analysis is UU-P07 (Amaru, 2007).

1  
2  
3  
4  
5  
6  
7  
8  
9  
10  
11  
12  
13  
14  
15  
16  
17  
18  
19  
20  
21  
22  
23  
24  
25  
26  
27  
28  
29  
30  
31  
32  
33  
34  
35  
36  
37  
38  
39  
40  
41  
42  
43  
44  
45  
46  
47  
48  
49  
50  
51  
52  
53  
54  
55  
56  
57  
58  
59  
60  
61  
62  
63  
64  
65

(Ryukyu vs. Izu-Bonin-Mariana trenches; (Faccenna et al., 2018; Hall and Spakman, 2002)), as well as from paleo-reconstructions, e.g., Trans-Tethyan System (Jagoutz et al., 2015), and Late Cretaceous eastern Turkey evolution (Eyuboglu et al., 2019). The double-subduction model has recently received much attention to address the problem of enigmatic slab kinematics encountered at both modern and ancient convergent zones (Čížková and Bina, 2015; Dasgupta and Mandal, 2018; Jagoutz et al., 2015). Based on seismic tomography and available plate kinematics data from GPS observations, three types of double-subduction configurations (Király et al., 2021) have been recognized: outward-, inward- and same-dipping slabs (Fig. 1). This study, however, explores the complex dynamics of same-dip double subduction with a focus on the Neo-Tethyan tectonic evolution.

Plate reconstruction studies suggest that same-dip double subduction (SDDS) systems developed repeatedly in the course of the ~150 Myr Neo-Tethyan evolutionary history (Hall, 2012; Kufner et al., 2016; Pusok and Stegman, 2020). Using quantitative models, Jagoutz et al. (2015) have shown the existence of coupled subduction zones in the Trans-Tethyan intra-oceanic system below the southern margin of Eurasia. During the Cretaceous to Early Tertiary period, this tectonic system evolved through multiple Neo-Tethyan subduction episodes, featuring the Kshiroda Plate's north-dipping oceanic slab under Eurasia (Yin and Harrison, 2000) and intra-oceanic subduction of the northern oceanic segment of the Indian subcontinent beneath the Kshiroda Plate leading to the formation of the Kohistan extensional arc. Geological, geochemical, and paleomagnetic investigations in the tectonic units, specifically the forearc, oceanic melange, and ophiolite sequences of the Himalayas (Aitchison et al., 2000; Bouilhol et al., 2013; Hall, 2012; Yin and Harrison, 2000) imply the concurrence of parallel subduction zones with similar dipping orientations. Complementing these findings, geophysical observations, such as the detection of

1  
2  
3  
4 66 multiple slab remnants through seismic tomography models (Van Der Voo et al., 1999), and  
5  
6 67 alterations in trench kinematics and the upper plate's deformation patterns (Gürer et al., 2016;  
7  
8 68 Jolivet et al., 2018), further reinforce the argument in favour of SDDS. Similarly, recent works  
9  
10 69 have recognized multiple double-subduction events to reconstruct the evolution of the Andaman  
11  
12 70 Subduction system (Advokaat et al., 2018; Bandyopadhyay et al., 2020; Ghosh et al., 2017). Its  
13  
14 71 active tectonics now occurs at the northern flank of the Java trench where the oceanic part of the  
15  
16 72 Indian Plate subducts at a low angle to the arc-trend beneath the overriding Andaman  
17  
18 73 microcontinental block. Geochronological correlations and geochemical signatures of the arc-  
19  
20 74 volcanism (Westerweel et al., 2019) and ophiolitic suites (Acharyya et al., 1991) indicate the  
21  
22 75 activity of a second subduction zone on the eastern side in late-Miocene, continuing to present day.  
23  
24 76 Also, geochemical evidence (Ghosh et al. 2017) suggests that the Andaman-Nicobar outer-arc high  
25  
26 77 grew from the coalescence of two accretionary prisms linked to the double-subduction tectonics.  
27  
28 78 Despite a significant advancement of their geochemical and geophysical information, there  
29  
30 79 remains a necessity of dynamically self-consistent geodynamic models to conceptualize the  
31  
32 80 following unresolved tectonic issues of these SDDS systems: 1) the unusually high Late  
33  
34 81 Cretaceous Indo-Eurasian subduction velocity, although the Kohistan extensional zone reduced  
35  
36 82 the transfer of pull force from front to rear slab, 2) reconstruction of the Andaman Convergent  
37  
38 83 System in the framework of Neo-Tethyan tectonics, and 3) dynamic backdrop of the failed trench  
39  
40 84 at Amirante and its relationship to the Cenozoic Indo-Eurasian subduction. This study aims to  
41  
42 85 develop SDDS models, mainly to address these long-standing issues of the Neo-Tethyan tectonics.  
43  
44  
45  
46  
47  
48  
49  
50  
51  
52

53 86 Recent analogue and numerical modelling have dealt with the complexities in double-  
54  
55 87 subduction evolution and their effects on the regional plate motion, intraplate deformations, slab  
56  
57 88 interactions and topographic developments (Dasgupta and Mandal, 2018; Holt et al., 2017; Király  
58  
59  
60  
61  
62  
63  
64  
65

1  
2  
3  
4  
5  
6  
7  
8  
9  
10  
11  
12  
13  
14  
15  
16  
17  
18  
19  
20  
21  
22  
23  
24  
25  
26  
27  
28  
29  
30  
31  
32  
33  
34  
35  
36  
37  
38  
39  
40  
41  
42  
43  
44  
45  
46  
47  
48  
49  
50  
51  
52  
53  
54  
55  
56  
57  
58  
59  
60  
61  
62  
63  
64  
65

89 et al., 2021; Mishin et al., 2008; Peral et al., 2018; Pusok and Stegman, 2019). It is now a well-  
90 established fact that their mode of development significantly differs from that of a single-  
91 subduction system. The additional complexity originates primarily from inter-slab interactions that  
92 greatly influence the plate bending and viscous dissipation in the mantle, coupled with additional  
93 factors, such as contrasting plate ages, plate dimensions, rheology, and inter-slab distance (Čížková  
94 and Bina, 2015; Dasgupta and Mandal, 2018; Holt et al., 2017). The initial relative arrangement  
95 of tectonic plates is another influential factor in the double-subduction evolution. For instance,  
96 the Ryukyu-IBM system has an intra-oceanic subduction zone coupled with another subduction  
97 zone at an ocean-continent convergence boundary. In contrast, the Trans-Tethyan double  
98 subduction formed with the Indian continental plate linked to the subducting oceanic counterpart.  
99 This difference in the initial plate arrangements might have led to their contrasting evolutionary  
100 paths, resulting in completely different tectonic histories of these two regions. However, how the  
101 initial plate configuration governs the dynamic evolution of a SDDS system is still an open-ended  
102 question, which the present article addresses in the context of the Neo-Tethyan subduction  
103 tectonics.

104 We develop geodynamic models to simulate the thermo-mechanical evolution of SDDS  
105 systems, initiated along pre-existing lithospheric weaknesses and reconstruct the tectonic history  
106 of both the Indo-Eurasian and Andaman double subduction systems. The models are designed to  
107 reproduce time-dependent and self-consistently evolving subduction for a given plate  
108 configuration. This modelling allows to address the following key questions: 1) can two adjacent  
109 same-dip subduction zones grow concurrently, and 2) if so, how do these neighbouring subduction  
110 zones mutually influence each other during their evolution, depending on their initial tectonic  
111 configurations? We also explore the following influential phenomena: a) mutual interactions of

1  
2  
3  
4  
5  
6  
7  
8  
9  
10  
11  
12  
13  
14  
15  
16  
17  
18  
19  
20  
21  
22  
23  
24  
25  
26  
27  
28  
29  
30  
31  
32  
33  
34  
35  
36  
37  
38  
39  
40  
41  
42  
43  
44  
45  
46  
47  
48  
49  
50  
51  
52  
53  
54  
55  
56  
57  
58  
59  
60  
61  
62  
63  
64  
65

112 simultaneous subducting-slab motions during the evolution of commonly reported Neo-Tethyan  
113 SDDS systems, b) complexity in the associated mantle flow patterns and their role in localization  
114 of lithospheric-scale extensional zones in convergent tectonics, and c) slab detachment leading to  
115 a double- to single-subduction transition.

## 2. Numerical Modelling Approach

### 2.1. Model Design

We use 2D thermomechanical numerical models (Fig. 2) that are inherently dynamic, implying  
that no external forces or velocities are applied to the overall system. Details of the numerical  
method and model boundary conditions are provided in Appendix A. The model domain represents  
a rectangular 7000 km (horizontal) x 1000 km (depth) vertical section (Fig. 2a). We introduce  
mechanical weaknesses in the lithospheric layer, as considered in previous studies that suggested  
spontaneous subduction initiation to occur preferentially at the locations of pre-existing  
lithospheric weakness, e.g., transform faults (Arcay et al., 2020; Zhou et al., 2018). This weak-  
zone perturbation for subduction initiation is a viable mechanical model in the light of damage  
theory proposed by Bercovici & Ricard, 2014. Our model implements this weakness as a narrow  
(10 km wide), low-viscosity ( $10^{20}$  Pa s) zone, extending to the lithospheric base (Fig. 2). The weak  
zones can also characterize intraplate lithosphere-scale faults in large oceanic plates, like the

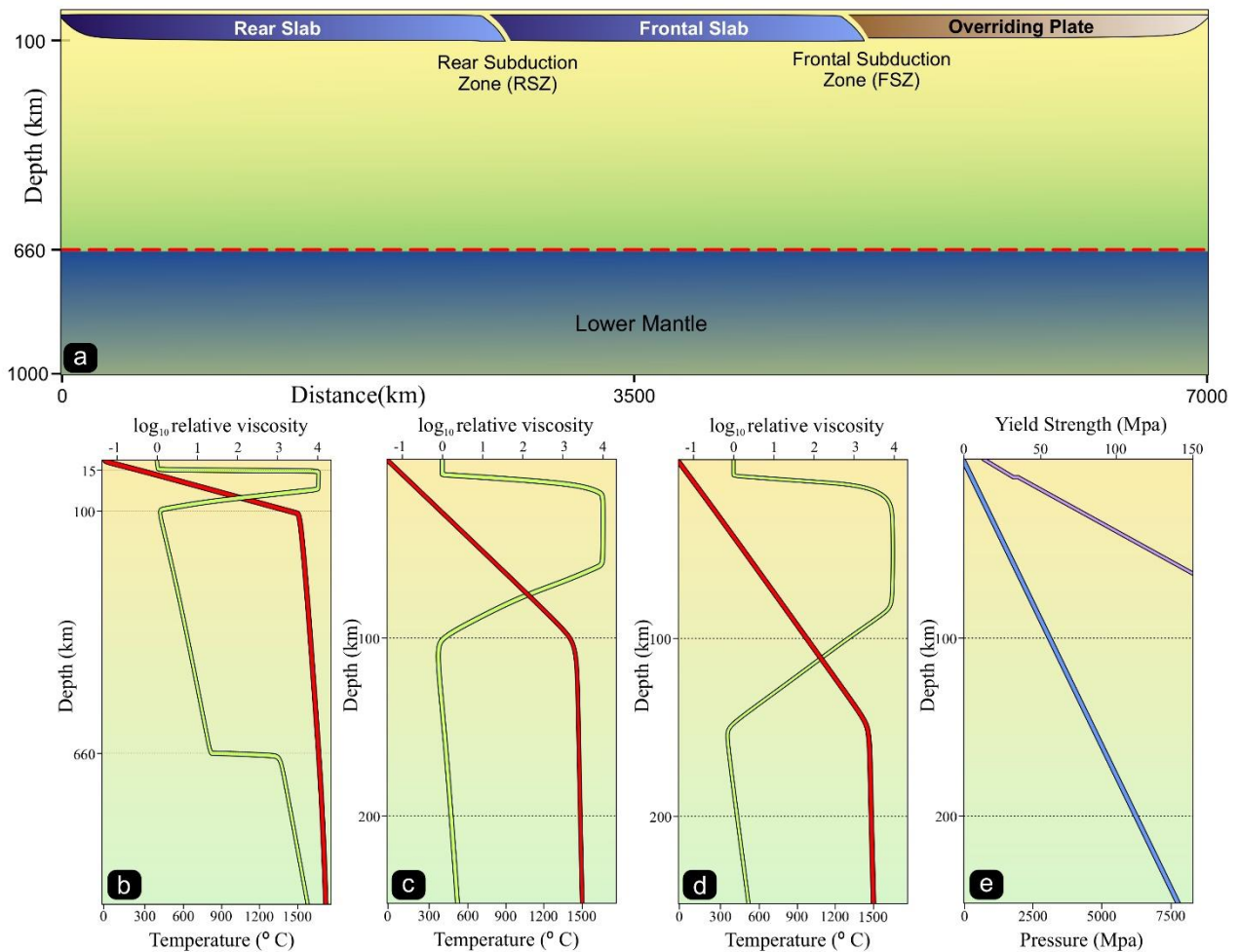


Figure 2: (a) The model setup and boundary conditions considered for CFD simulations, which shows the whole domain and initial setup of model employed for simulating same-dip double subduction in oceanic setting. Detailed illustrations representing the viscosity and temperature profiles of b) the complete model domain, c) oceanic lithosphere, and d) continental lithosphere utilized in the models. The viscosity values are relative to the asthenosphere value of  $10^{20}$  Pa s. e) The strength plots exhibiting depth-dependent variations, showcasing increasing strength (purple) and pressure (blue).

129 present-day Wharton Basin (Stevens et al., 2020). All the rheological and thermal parameters used

130 in this study are summarized in Table 1.

## 131 2.2. Model Configurations

132 Natural subduction zones occur in various convergent settings, which can be broadly  
 133 categorized as: 1) oceanic settings (e.g., Izu-Bonin-Mariana), where two or more oceanic plates  
 134 converge to each other; 2) ocean – continent settings (e.g., the Andean subduction system), where  
 135 oceanic plates converge against continents; and 3) continent-continent settings (e.g. the Indo-

1  
2  
3  
4  
5  
6  
7  
8  
9  
10  
11  
12  
13  
14  
15  
16  
17  
18  
19  
20  
21  
22  
23  
24  
25  
26  
27  
28  
29  
30  
31  
32  
33  
34  
35  
36  
37  
38  
39  
40  
41  
42  
43  
44  
45  
46  
47  
48  
49  
50  
51  
52  
53  
54  
55  
56  
57  
58  
59  
60  
61  
62  
63  
64  
65

136 Eurasia collisional zone), where two or more continents approach each other. Considering Earth's  
137 present-day plate structures, SDDS systems can develop in any of these three tectonic settings,  
138 giving rise to a spectrum of their potential plate configurations. Based on the paleo-reconstructions  
139 of the Neo-Tethyan tectonics, we thus chose three different cases for the model settings, with an  
140 objective to investigate the mode of double-subduction evolution depending on the initial plate  
141 architecture. Each of these initial settings accounts for local lithospheric weaknesses in a specific  
142 arrangement with or without mechanically strong continental blocks.

143         The first case of our subduction modelling (referred to as *oceanic plate model*) replicates a  
144 simple oceanic plate tectonic setting, consisting of a 120 Myr old, flat lying oceanic lithosphere  
145 with a length of 5000 km (Fig. 3a). The model initially contains two similarly-dipping narrow  
146 weak zones of different thicknesses in the oceanic lithospheric plates at distances of 2500 km and  
147 5000 km. The weak-zone configuration is chosen so that the model favours one of the weak zones  
148 to become active first to initiate an ocean-ocean subduction zone, as reported from natural SDDS,  
149 such as the Trans-Tethyan subduction system. No continent is included in the model domain to  
150 exclusively show the effects of oceanic plates on the SDDS dynamics. We also implement a  
151 corresponding single subduction model (Supplementary section S1) to find the additional effects  
152 of inter-slab interactions. The second case (referred to as *oceanic– continental plate model*) is  
153 designed to represent an ongoing subduction system, where an oceanic plate has already been  
154 subducted into the upper mantle, carrying a 400 km long and ~150 km thick microcontinental  
155 block (Fig. 4a). This configuration aims to reveal the mechanical effects of pre-existing micro-  
156 continent between two oceanic plates. The continental crust is assigned a compositional density  
157 lower than that of mantle material by 600 kg/m<sup>3</sup>. The block is assumed to form a weak interface  
158 with the adjoining oceanic plate, possibly resulting from the inter-plate 3D differential stress



1  
2  
3  
4 159 localization (Auzemery et al., 2020; Heidbach et al., 2007). On the rear side, it is separated from  
5  
6  
7 160 an 80 Ma old oceanic lithosphere by a dipping (30°) weak zone. The third model, designed to  
8  
9 161 reproduce a continent-continent collisional setting (referred to as *multiple continent model*),  
10  
11 162 initially consists of a flat-lying 1200 km long, 80 Myr old oceanic lithosphere, and two continental  
12  
13  
14 163 blocks (thickness: 150 km and length: 1500 km), separated by an oceanic basin. This oceanic plate  
15  
16 164 forms a narrow weak channel at the contact with the overriding strong continental plate (Fig. 5a).  
17  
18  
19 165 The continental blocks are compositionally buoyant relative to the underlying asthenosphere.  
20

### 21 166 **3. Model results**

#### 22 167 *3.1. Oceanic plate settings*

23  
24 168 This model setting localizes plastic yielding preferentially at one of the pre-existing  
25  
26  
27 169 lithospheric weaknesses (Fig.3a), resulting in an unstable state of the flat-lying oceanic plate to  
28  
29  
30 170 initiate the rear subduction zone (RSZ). This process accompanies the formation of a divergent  
31  
32  
33 171 spreading centre that eventually acts as an active site of oceanic plate generation. At ~6 Myr, the  
34  
35  
36 172 newly generated lithosphere constitutes a well-developed overriding plate (OP) structure in the  
37  
38  
39 173 subduction zone. The proto-slab subducts to a depth of ~300 km with a convergence rate ( $V_C$ ) of  
40  
41  
42 174 ~13 cm/yr (relative to its adjoining overriding oceanic plate) at 8.1 Myr (Fig 3b). The active RSZ  
43  
44 175 plate approaches the trench with a velocity ( $V_P$ ) of ~+12 cm/year (+ sign denotes movement  
45  
46  
47 176 towards the right), while the trench itself retreats with a velocity ( $V_{RT}$ ) of ~-2.5 cm/yr. The plate  
48  
49 177 convergence velocity (calculated between passive markers 1 and 3; Fig. 3a) accelerates further  
50  
51 178 with increasing total negative buoyancy to attain a maximum value of ~15 cm/year (Fig. 6a), and  
52  
53  
54 179 the RSZ slab dip (measured at 125 km depth) steepens to ~45°. The slab subsequently encounters  
55  
56 180 the 660-km transition at 10.1 Myr, and decelerates ( $V_P \approx 7.5$  cm/yr) due to higher viscous resistance  
57  
58  
59  
60  
61  
62  
63  
64  
65

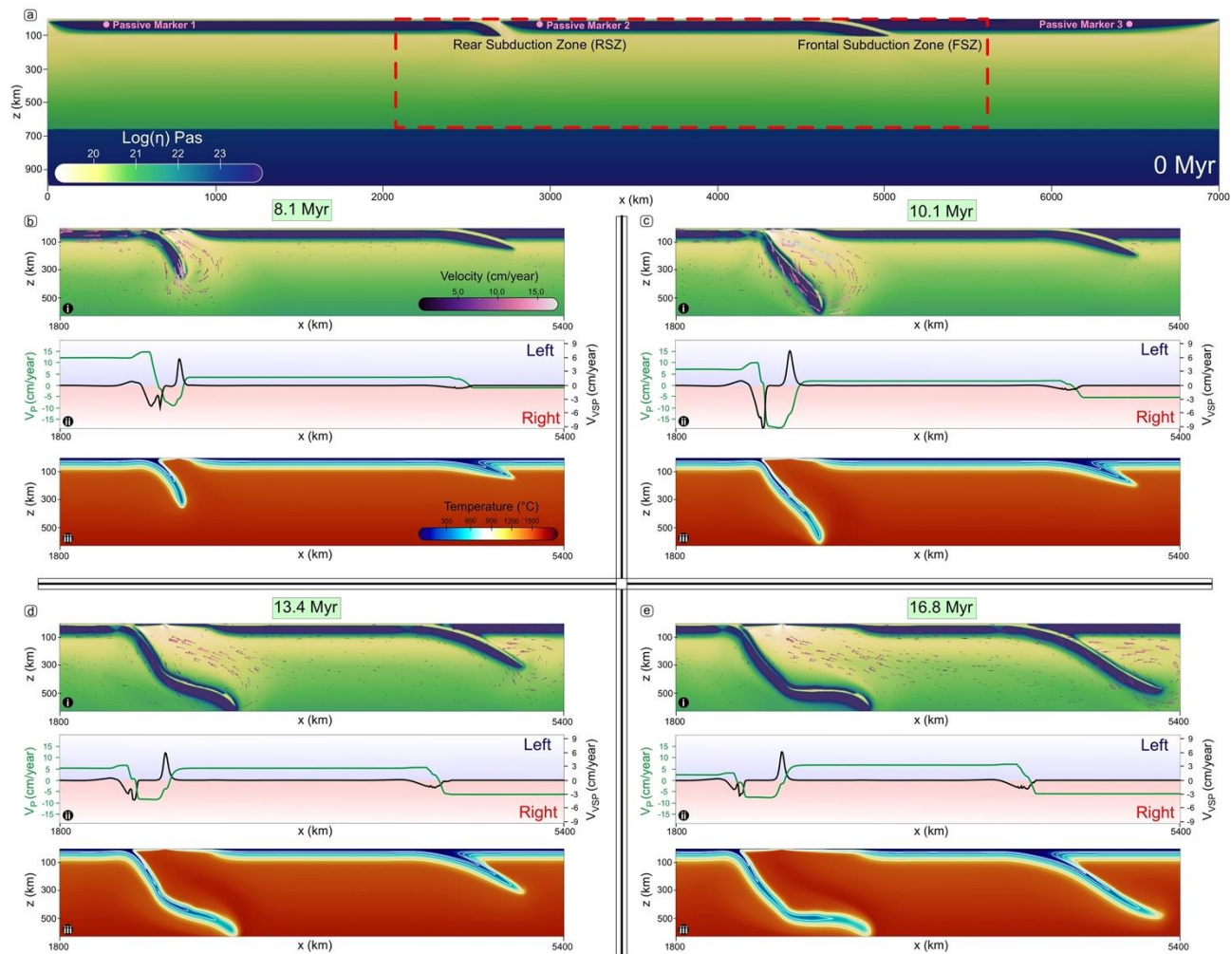


Figure 3: Evolution of the double subduction model in an oceanic setting. Panels show: (a) the initial viscosity field of the complete numerical model domain, (b)-(e) evolution of the i) viscosity and velocity fields, ii) plate velocities ( $V_P$ ) (green) and vertical subduction-velocity ( $V_{VSP}$ ) (black), which denote the horizontal ( $V_x$ ) and vertical ( $V_y$ ) component of the total velocity vector respectively, and iii) temperature field, zoomed into a region around the subduction zone for four time-steps corresponding to the back subduction initiation ( $t= 8.1$  Ma), frontal subduction initiation ( $t= 10.1$  Ma), frontal subduction free sinking ( $t= 13.4$  Ma) and mature double subduction ( $t = 16.8$  Ma) phases.

181 in the stronger lower mantle. This slab-lower mantle interaction also forces the oceanic plate to  
 182 slow down its motion ( $V_c \approx 12$  cm/year; Fig. 6a), prompting the other proto-slab to activate and  
 183 initiate the frontal subduction zone (FSZ) (Fig. 3c). At this stage, the tectonic setting transforms  
 184 into a typical double-subduction configuration, albeit with significant asymmetry in terms of both  
 185 slab geometry and kinematics, where the FSZ slab shows much shallower dip ( $\sim 20^\circ$ ) and lower  
 186 convergence velocity ( $V_c^{RS} \approx 7$  cm/yr) than the rear subducting slab. Additionally, the RSZ trench

1  
2  
3  
4 187 retreats significantly faster ( $V_{RT} \approx 9$  cm/yr) than the FSZ trench ( $V_{FT} \approx 2.5$  cm/yr). The cumulative  
5  
6  
7 188 effects of double-subduction motion facilitate the convergence motion to not only attain, but also  
8  
9 189 sustain extremely high velocities for a prolonged period ( $\sim 6$  Myr). This is in stark contrast to  
10  
11  
12 190 scenarios of single subduction, where such extreme convergence rates can prevail over short  
13  
14 191 durations ( $< 1$  Myr).

15  
16 192         The double-subduction system always maintains an active state of the spreading centre to  
17  
18  
19 193 continuously produce new lithospheric materials. At  $\sim 13.4$  Myr, the RSZ attains a declining stage,  
20  
21 194 marked by a significant drop in  $V_P$  ( $\sim 5$  cm/yr), although its trench continues to retreat with  $V_{RT} \sim 3$   
22  
23 195 cm/yr. In contrast, the FSZ continues to remain active, with its slab sinking rapidly into the upper  
24  
25  
26 196 mantle to facilitate the convergence velocity ( $V_P \approx 5$  cm/year) as well as the trench retreat velocity  
27  
28 197 ( $V_{FT} \approx 7$  cm/year). However, the SDDS system cumulatively shows a decreasing trend of the net  
29  
30  
31 198 convergence velocity ( $V_c \approx 11$  cm/yr). At  $\sim 16.8$  Myr, the rear subducting slab moves backward as  
32  
33 199  $V_{RT}$  ( $\sim 3.5$  cm/year) exceeds  $V_P$  ( $\sim 2.5$  cm/year) and the double-subduction evolves to a steady state  
34  
35  
36 200 condition of the RSZ in terms of  $V_c$  and slab dip ( $\sim 55^\circ$ ). On the opposite side, however, the oceanic  
37  
38 201 plate associated with the FSZ acquires a maximum velocity  $V_P \approx 6.5$  cm/year, significantly higher  
39  
40  
41 202 than the rear subducting plate velocity. The FSZ slab then moves through the entire upper mantle  
42  
43 203 to encounter the lower mantle and eventually slows down its velocity. The corresponding trench  
44  
45 204 continues to retreat with  $V_{FT} \approx 6$  cm/yr, which subsequently surpasses the FSZ plate velocity in  
46  
47  
48 205 course of the subduction evolution ( $> 20$  Myr). The convergence attains a velocity of  $\sim 8.5$  cm/year  
49  
50 206 with a tectonically-steady configuration till the end of the model run.

51  
52  
53 207         During the RSZ-initiation stage, the descending-slab driven mantle flows exhibit both  
54  
55 208 vertical and horizontal components, shaping a circulating flow vortex around the subducted slab.  
56  
57  
58 209 The vortex remains active till  $\sim 10$  Ma, gradually waning as the RSZ slab decelerates upon  
59  
60  
61  
62  
63  
64  
65

1  
2  
3  
4  
5  
6  
7  
8  
9  
10  
11  
12  
13  
14  
15  
16  
17  
18  
19  
20  
21  
22  
23  
24  
25  
26  
27  
28  
29  
30  
31  
32  
33  
34  
35  
36  
37  
38  
39  
40  
41  
42  
43  
44  
45  
46  
47  
48  
49  
50  
51  
52  
53  
54  
55  
56  
57  
58  
59  
60  
61  
62  
63  
64  
65

210 encountering the 660 km discontinuity. With this deceleration, the vortex's focal point shifts to the  
211 FSZ slab, accompanied by an increasing flow intensity with time. At ~13 Myr, the double-  
212 subduction configuration sets in a potent upward slab-parallel flow beneath the spreading centre,  
213 which strengthens further by merging with the counter-flow generated by the frontal subducting  
214 slab (Fig. 3e-i). Together, these components constitute a robust mechanism for channelling mantle  
215 materials towards the spreading centre. Notably distinct from typical single-subduction driven  
216 corner and wedge flows, this increased mantle-material supply emerges as a pivotal factor to  
217 facilitate the accretion rates of lithosphere.

### 3.2. *Microcontinent - oceanic plate setting*

219 The micro-continent-bearing oceanic plate setting consists of an already initiated subduction  
220 in the front (FSZ: frontal subduction zone) and the lithospheric weakness between the  
221 microcontinent. This configuration results in initiation of the rear subduction zone, forming a  
222 double-subduction system at an early stage (~6 Myr) of the model run (Fig.4b), as evident from a  
223 convergence velocity  $V_C \approx 5$  cm/yr (Fig. 6b). The subduction zones, however, grow at different  
224 rates, where the FSZ subduction is much more active than the RSZ. This difference in their  
225 subduction rates causes rifting between the FSZ oceanic plate and the microcontinent. The rift  
226 subsequently acts as a spreading centre, allowing upwelling of the underlying mantle material to  
227 the surface and generate new oceanic lithosphere between the continental and the frontal oceanic

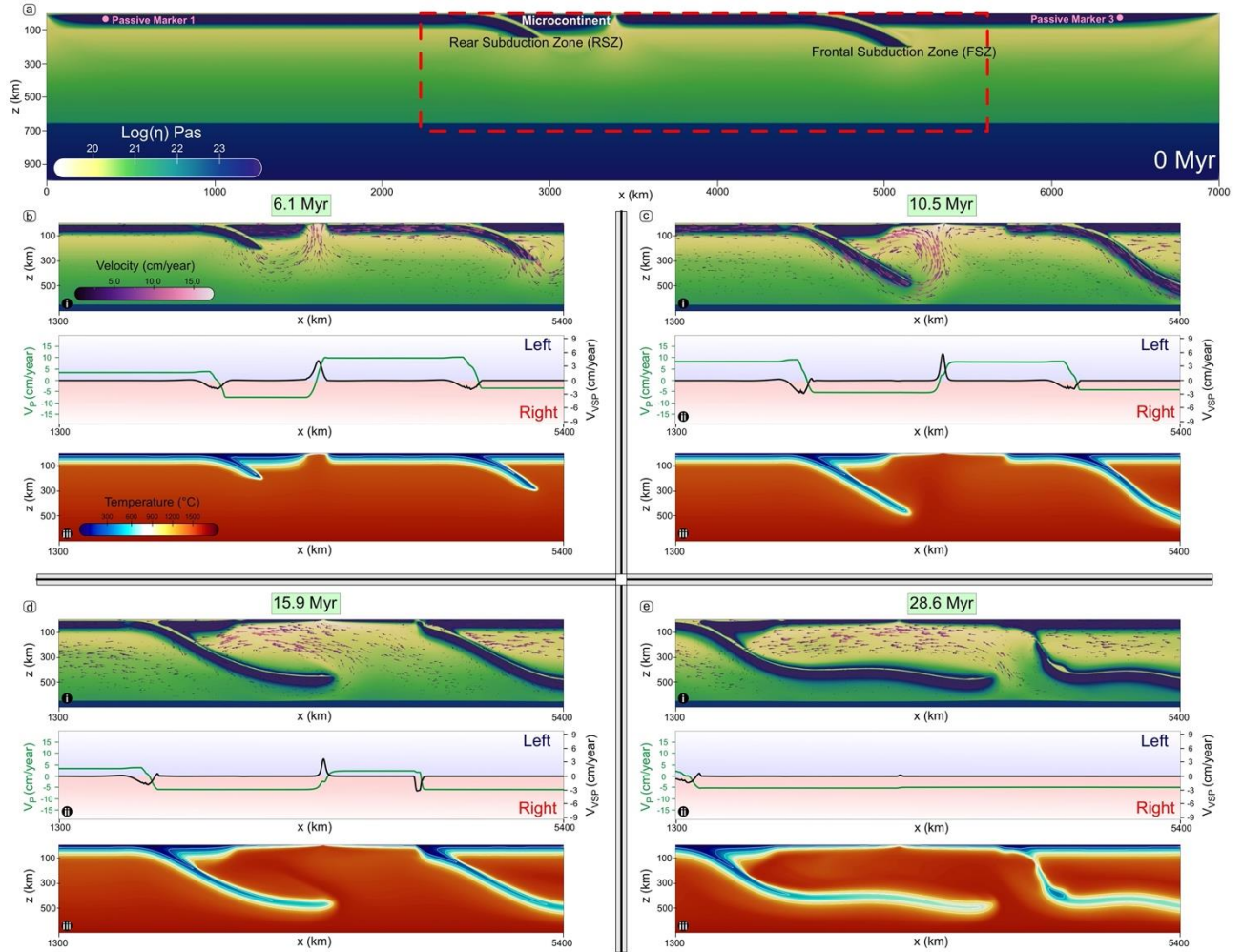


Figure 4: Evolution of the double subduction model in presence of a continental block. Panels show: (a) the initial viscosity field of the complete numerical model domain, (b)-(e) evolution of the i) viscosity and velocity fields, ii) plate velocities ( $V_P$ ) (green) and vertical subduction-velocity ( $V_{VSP}$ ) (black), which denote the horizontal ( $V_x$ ) and vertical ( $V_y$ ) component of the total velocity vector respectively, (see Supplementary section S2) and iii) temperature field, zoomed into a region around the subduction zone for four time-steps corresponding to the fore subduction free sinking ( $t = 6.1$  Ma), back subduction free sinking ( $t = 10.5$  Ma), mature double subduction ( $t = 15.9$  Ma) and fore subducting slab detachment ( $t = 28.6$  Ma) phases.

At  $\sim 6.1$  Myr, the RSZ proto-slab subducts to a depth of  $\sim 200$  km into the upper mantle, and this subduction motion forces the continental block to act as an OP, moving trench-ward at a velocity  $V_P \sim -7$  cm/year. The FSZ slab, on the other side, continues to subduct freely into the upper mantle, setting the entire plate to move at a high velocity ( $V_P \sim +10$  cm/yr) (Fig. 4a). During this phase of tectonic evolution both the trenches retreat, but with contrasting velocities; the RSZ trench

1  
2  
3  
4  
5  
6  
7  
8  
9  
10  
11  
12  
13  
14  
15  
16  
17  
18  
19  
20  
21  
22  
23  
24  
25  
26  
27  
28  
29  
30  
31  
32  
33  
34  
35  
36  
37  
38  
39  
40  
41  
42  
43  
44  
45  
46  
47  
48  
49  
50  
51  
52  
53  
54  
55  
56  
57  
58  
59  
60  
61  
62  
63  
64  
65

retreats at a significantly faster rate ( $V_{RT} \approx -6.5$  cm/yr) than the FSZ ( $V_{FT} \approx -3.8$  cm/yr). The convergence velocity between the main OP and the RSZ slab is  $\approx 7$  cm/year, which increases to a high value ( $V_C \approx 13$  cm/yr) on a model run time of  $\sim 9$  Myr (Fig. 6b). The frontal oceanic slab reaches the lower mantle at  $\sim 10.5$  Myr and begins to slow down the velocity ( $V_P \approx +7$  cm/yr) due to higher viscous forces in the 660-km transition zone. The RSZ slab, however, continues to subduct through the upper mantle and maintains the rear oceanic plate movement at a velocity of  $\approx +8$  cm/year. The RSZ trench at the same time retreats, but with a reduced velocity ( $V_{RT} \approx -5$  cm/yr), whereas the FSZ trench continues to retreat at a steady rate ( $V_{FT} \approx -4$  cm/year). The convergence velocity is high ( $V_C \approx 13$  cm/year), but shows a diminishing trend after this period. At  $\sim 15.9$  Myr, both the subducting oceanic slabs lower their dips to become almost flat, and significantly reduce the plate velocities ( $V_P \approx +2.5$  cm/yr and  $\approx +3.5$  cm/yr for FSZ and RSZ slabs, respectively). The relatively buoyant juvenile ( $\sim 15$  Myr) lithosphere, formed at the spreading centre, eventually reaches the FSZ trench and its subduction accelerates the retreat motion ( $V_{FT} \approx +7.5$  cm/year). This motion reduces its slab dip from  $30^\circ$  to  $\sim 26^\circ$  (Fig. 6b), which starts to increase significantly after  $\sim 18$  Myr. The RSZ trench retreat velocity ( $V_{RT}$ ) increases to  $-5.5$  cm/yr during this period. At  $\sim 25$  Myr, the FSZ slab undergoes break-off at the location of maximum strain localisation developed by the negative buoyancy induced slab pull (see Supplementary S3 for detailed strain-rate plots).

In this SDDS system, the spreading centre located between the two trenches remains active, continuously adding new lithosphere to accommodate the increasing space between the continental block and the frontal oceanic plate. At  $\sim 28.6$  Myr, the spreading centre, however, becomes almost inactive as the upwelling process is replaced by slab-driven horizontal flows in the mantle region between the two subducting plates. The entire newly formed lithosphere is coherently coupled with

1  
2  
3  
4  
5  
6  
7  
8  
9  
10  
11  
12  
13  
14  
15  
16  
17  
18  
19  
20  
21  
22  
23  
24  
25  
26  
27  
28  
29  
30  
31  
32  
33  
34  
35  
36  
37  
38  
39  
40  
41  
42  
43  
44  
45  
46  
47  
48  
49  
50  
51  
52  
53  
54  
55  
56  
57  
58  
59  
60  
61  
62  
63  
64  
65

the main OP, as revealed from the plate velocity ( $V_P \approx -5$  cm/year). The double subduction system ceases to exist due to the absence of slab pull force at the FSZ trench and transforms into a single subduction system.

### 3.3. Multiple-continental plate setting

The model run shows that subduction localizes preferentially along the lithospheric weakness to initiate the frontal subduction zone (FSZ), leaving the trailing weak zone at the continent-oceanic plate interface almost inactive (Fig. 5b). At this stage ( $\sim 4$  Myr) the system follows mostly single-subduction dynamics, allowing the FSZ slab to penetrate into the upper mantle to a depth of  $\sim 200$  km. The plate velocity ( $V_P$ ) increases to  $\sim +7.5$  cm/year on a model run time of 8.5 Myr (Fig. 5b). The velocity field indicates that the lithospheric plates move coherently as a single unit to subduct beneath the FSZ trench although a lithospheric weakness is present in between them ( $V_P \approx +5$  cm/year for rear oceanic plate). This implies that the FSZ entirely determines the dynamics of the system at an early stage. The frontal oceanic plate progressively accelerates its motion to attain a convergence rate ( $V_c^{RS} \approx 8$  cm/year, Fig. 6c solid blue line) with respect to the OP at  $\sim 11.5$  Myr. At this stage the subduction system undergoes a remarkable kinematic transformation, leading to plate decoupling at the rear lithospheric weakness that eventually triggers mantle upwelling and accretion of new lithospheric materials to form a thin overriding plate. This decoupling decelerates the rear plate motion ( $V_P \approx +1$  cm/year) and brings it almost to a halt. In contrast, the frontal slab continues to maintain a high plate velocity ( $V_P \approx +7.5$  cm/year) and a high convergence rate ( $V_c^{RS} = +7.5$  cm/year), along with a moderate trench retreat rate ( $V_{FT} \approx -3.5$  cm/yr). At  $\sim 12.5$  Myr, the rear subducting slab gains a significant slab-pull velocity ( $V_{SP} \approx -10$  cm/year), which consequently causes initiation of the rear subduction zone (RSZ). The proto-slab continues to move through the upper mantle, setting the convergence velocity rapidly

1  
2  
3  
4  
5  
6  
7  
8  
9  
10  
11  
12  
13  
14  
15  
16  
17  
18  
19  
20  
21  
22  
23  
24  
25  
26  
27  
28  
29  
30  
31  
32  
33  
34  
35  
36  
37  
38  
39  
40  
41  
42  
43  
44  
45  
46  
47  
48  
49  
50  
51  
52  
53  
54  
55  
56  
57  
58  
59  
60  
61  
62  
63  
64  
65

279 accelerate to attain a value of  $\sim 11$  cm/year at 13.8 Myr. On the other side, the FSZ slab reaches the  
 280 660-km transition zone and slows down its overall sinking velocities. The continental block in this  
 281 plate reaches the trench and collides with the overriding plate, switching a reversal in the trench  
 282 motion to advance at a rate  $V_{FT} \approx +2$  cm/yr. The collision event also reduces the plate velocity ( $V_P$   
 283  $\approx +5$  cm/yr) as well as the convergent velocity ( $V_c^{RS} \approx 4.5$  cm/yr) at  $\sim 15$  Myr. Eventually, the RSZ  
 284 experiences strong extensional forcing created by the FSZ, and its convergence reduces to

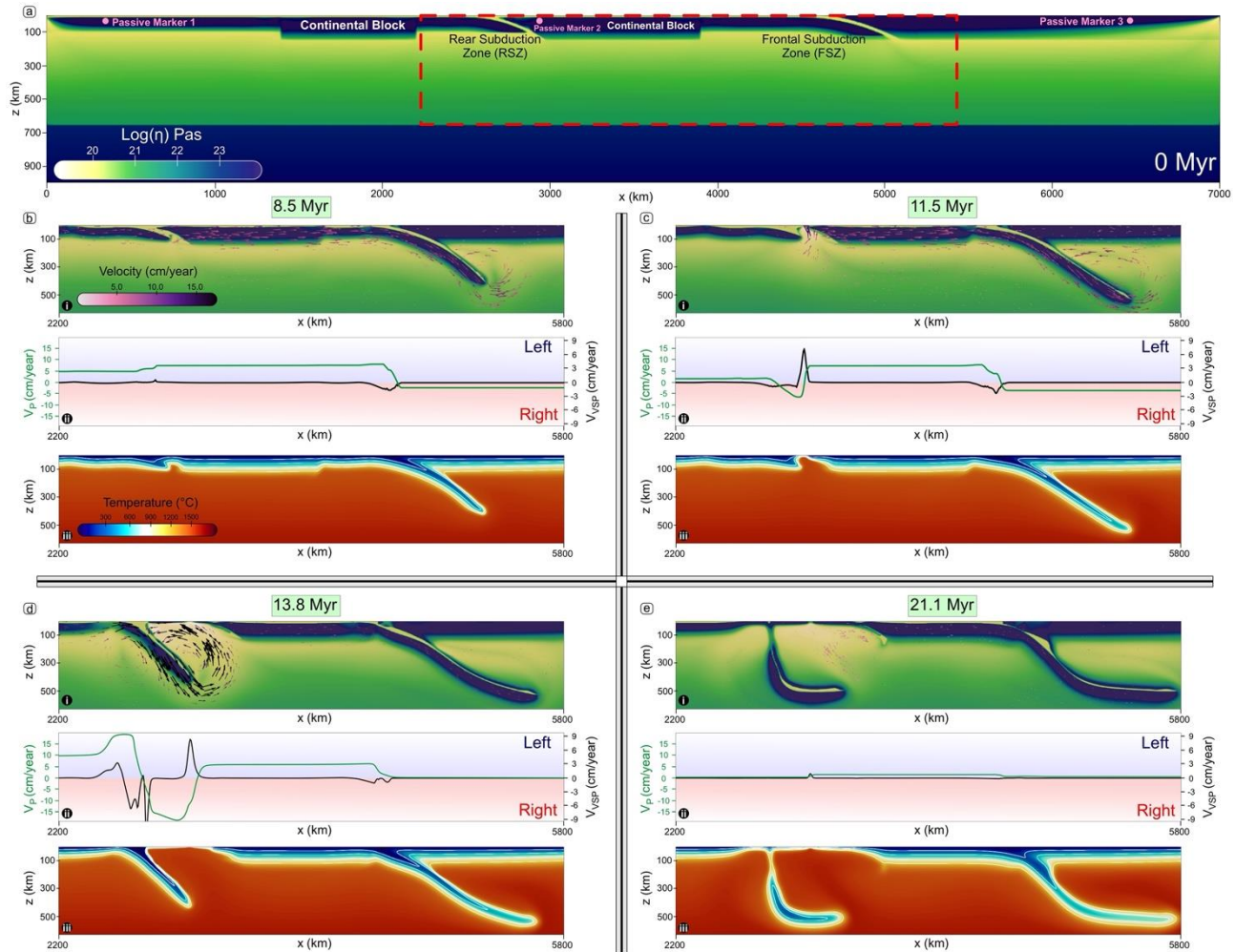


Figure 5: Evolution of the double subduction model in presence of multiple continental plates. Panels show: (a) the initial viscosity field of the complete numerical model domain, (b)-(e) evolution of the i) viscosity and velocity fields, ii) plate velocities ( $V_P$ ) (green) and vertical subduction-velocity ( $V_{VSP}$ ) (black), which denote the horizontal ( $V_x$ ) and vertical ( $V_y$ ) component of the total velocity vector respectively, and iii) temperature field, zoomed into a region around the subduction zone for four time-steps corresponding to the fore subduction free sinking ( $t = 8.5$  Ma), continental collision ( $t = 11.5$  Ma), back subduction initiation ( $t = 13.8$  Ma) and back subducting slab detachment ( $t = 21.1$  Ma) phases.



1  
2  
3  
4  
5  
6  
7  
8  
9  
10  
11  
12  
13  
14  
15  
16  
17  
18  
19  
20  
21  
22  
23  
24  
25  
26  
27  
28  
29  
30  
31  
32  
33  
34  
35  
36  
37  
38  
39  
40  
41  
42  
43  
44  
45  
46  
47  
48  
49  
50  
51  
52  
53  
54  
55  
56  
57  
58  
59  
60  
61  
62  
63  
64  
65

285 extremely low rates, which impedes the trench retreat, causing the RSZ slab to steepen ( $>65^\circ$ ) and  
286 eventually break off. The continental block plays an instrumental role to facilitate triggering the  
287 slab detachment at  $\sim 16$  Myr. In course of the double-subduction evolution ( $\sim 21.1$  Myr), the plate  
288 velocities drastically drop to  $\sim 2.5$  cm/year and the tectonic setting transforms into a single  
289 subduction system. Thus, these results show that in this SDDS system, two simultaneous  
290 subduction zones cannot be sustained and the subduction behind the collision zone ceases without  
291 attaining maturity.

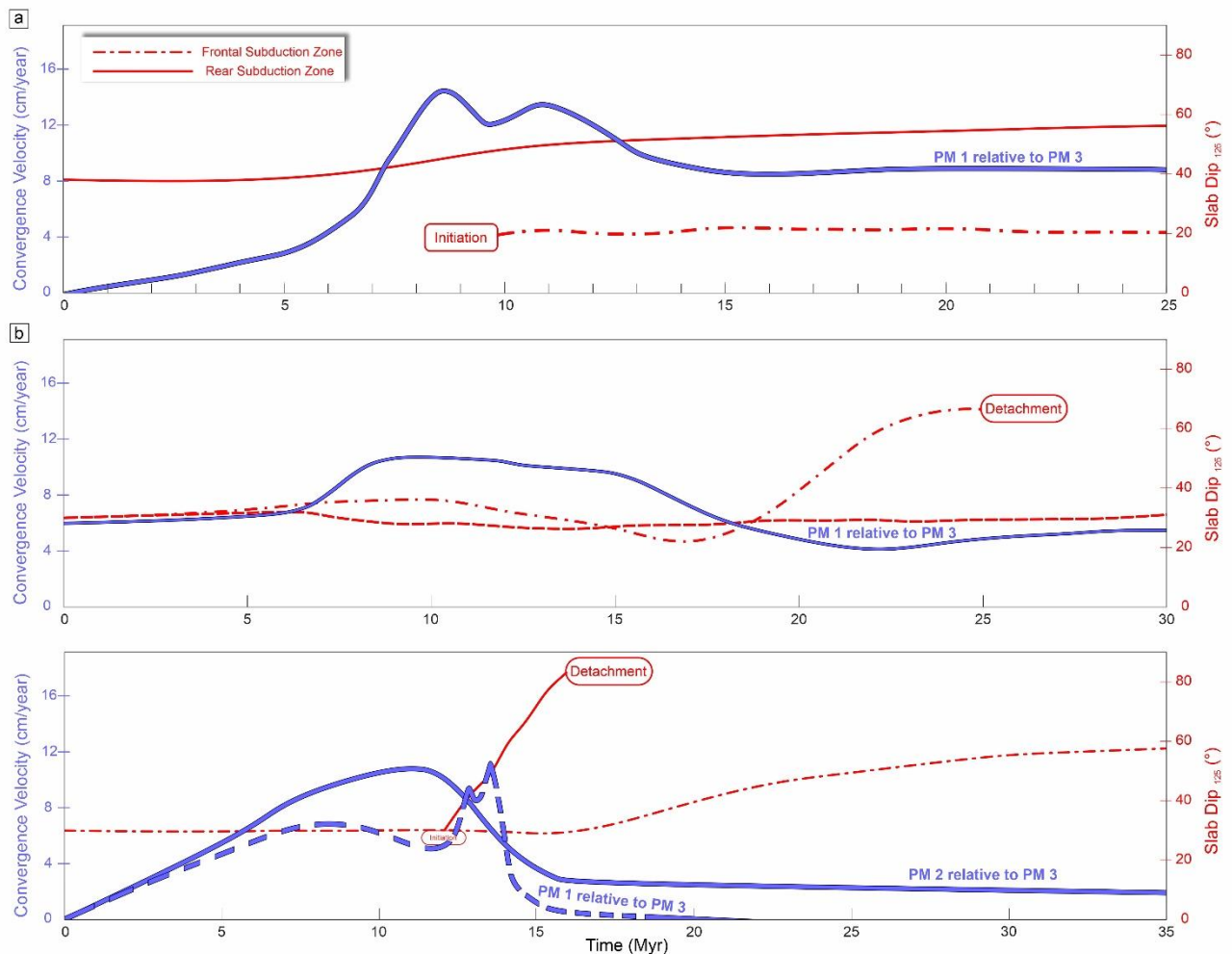


Figure 6: Temporal evolution of subduction zone convergence rates and shallow slab dips (at depth = 125 km) of fore and back subducting slabs, for double subduction in a) oceanic setting, b) microcontinent - oceanic plate setting and, c) multiple continental plate setting. PM: Passive Marker

## 292 4. Discussion

### 293 4.1. *Applicability of the double-subduction models to the Neo-Tethyan systems*

294 Based on the available field, petrological, paleo-magnetic and geochemical information,  
295 we consider the following Neo-Tethyan subduction systems: i) Trans-Tethyan intra-oceanic  
296 system, ii) India-Andaman-Burma subduction system, and iii) Amirante-India-Eurasia to discuss  
297 their evolution in the light of the present SDDS models. These subduction systems are chosen as  
298 their tectonic settings have been well-constrained by combining geological and geophysical  
299 observations in recent studies. Additionally, seismic observations indicate that the subducted slabs  
300 in these systems rested in the upper parts of the lower mantle (Van Der Voo et al., 1999; Yang et  
301 al., 2022). To implement this slab configuration in the simulations, our modelling excludes the  
302 phase changes at the 660-km transition.

#### 303 4.1.1. *Cretaceous evolution of the Trans-Tethyan System*

304 The Trans-Tethyan intra-oceanic system (Fig. 7a) evolved through multiple subduction  
305 episodes in the Neo-Tethys during the Cretaceous to Early Tertiary period as discussed earlier in  
306 Section 1. The convergence history, derived from the plate reconstructions and paleomagnetic  
307 interpretations (Cande and Stegman, 2011; Copley et al., 2010; Van Hinsbergen et al., 2011) reveal  
308 that, during the Indo-Eurasian convergence the Indian Plate had a rapid northward drift moving at  
309 extremely high velocities  $>12$  cm/year from 60 Ma to 50 Ma (Copley et al., 2010; Molnar & Stock,  
310 2009), which subsequently reduced to 8 cm/year at  $\sim 40$  Ma that marks the timing of India-Eurasia  
311 collision (Maiti et al., 2021). The oceanic plate model presented in Section 3.1 provides new  
312 insights into the geodynamic evolution of the Trans-Tethyan intra-oceanic system. The subducting  
313 oceanic plates in the model, RSZ and FSZ represent the frontal oceanic part of the Indian Plate

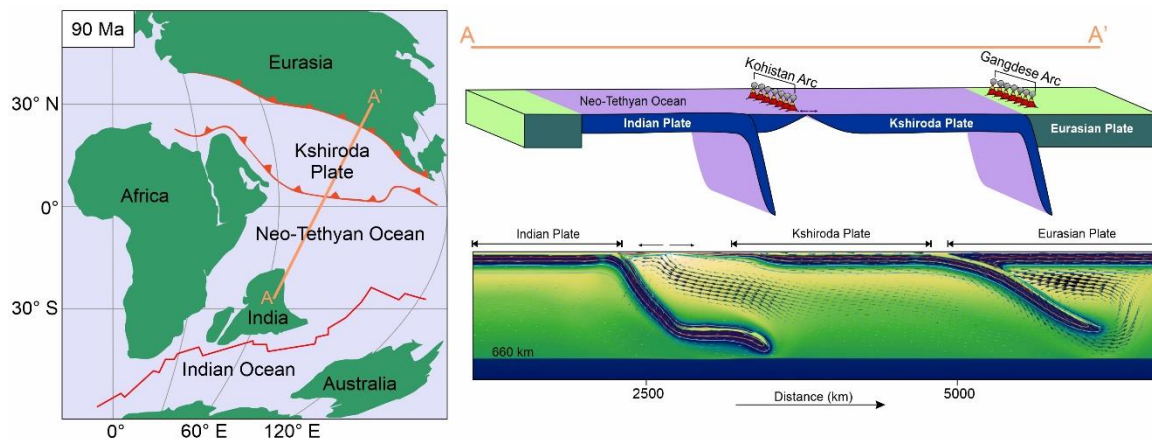


Figure 7: a) Sketch showing the reconstructions of Neo-Tethyan plate boundaries at ~90 Ma modified after Jagoutz et al., 2015 b) Cross section along AA' showing slab geometries and distances between the two prominent subduction systems giving rise to the double subduction process. c) Time snapshot (16 Myr) of the oceanic SDDS model which simulates the Cretaceous evolution of the Trans-Tethyan System.

314 and the Kshiroda Plate, respectively, in association with the Eurasian overriding plate (Fig 7a,b).  
 315 Pre-existing lithosphere-scale weaknesses, such as transform faults or oceanic fracture zones  
 316 between the Kshiroda and the Indian Plate nucleated the subduction initiation at the leading edge  
 317 of the Indian oceanic lithosphere, almost synchronously accompanied by opening of a proto back-  
 318 arc extensional zone. The subduction event resulted in arc formation, preserved as the Kohistan-  
 319 Ladakh Arc in the Himalaya-Tibet Mountain system (Bouilhol et al., 2013). A correlation of the  
 320 arc initiation timing with the paleomagnetic data reveal that the Kohistan–Ladakh Arc rocks and  
 321 ophiolites in the Tsangpo-suture zone formed nearly at the equator position (Aitchison et al., 2000).  
 322 After ~4-5 Myr from the intra-oceanic subduction initiation, the passive margin between the  
 323 Kshiroda and Eurasian Plates became active to form a second subduction (FSZ) (Fig. 7c), which  
 324 gave rise to the Gangdese-Karakoram continental arc. The paleomagnetic data of magmatic rocks  
 325 indicate that the arc formed at a latitudinal position ~20°–25° N, ~2500 km from the Kohistan Arc  
 326 present location, which is consistent with the present model estimates. The model convergence  
 327 history reveals a period of rapid convergence with velocities >~15 cm/year for a period of ~8 Myr

1  
2  
3  
4  
5  
6  
7  
8  
9  
10  
11  
12  
13  
14  
15  
16  
17  
18  
19  
20  
21  
22  
23  
24  
25  
26  
27  
28  
29  
30  
31  
32  
33  
34  
35  
36  
37  
38  
39  
40  
41  
42  
43  
44  
45  
46  
47  
48  
49  
50  
51  
52  
53  
54  
55  
56  
57  
58  
59  
60  
61  
62  
63  
64  
65

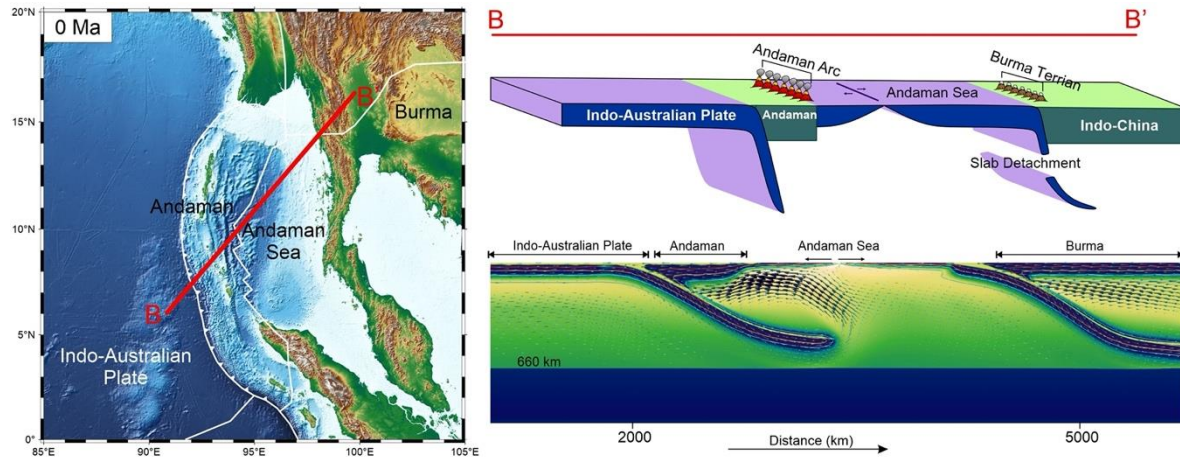
328 before reducing to ~9 cm/year in the later phase of the model run. This two-stage kinematic  
329 evolution is also in agreement with the Cretaceous convergence history of the Indo-Eurasian  
330 system prior to the Early Cenozoic slowdown (Molnar and Stock, 2009).

331 The existence of an extensional zone, namely the Kohistan Arc between two active  
332 subduction zones decoupled the oceanic plate, which in turn freed the rear slab from slab pull of  
333 the frontal subduction zone. According to this model, high convergence rates can originate in  
334 double subduction systems, even in the absence of any slab pull-force transfer from the frontal to  
335 the rear subduction zone. However, our model estimates yield the absolute Indian plate velocity  
336 (PM1: ~11-6 cm/year) lower than those interpreted from paleomagnetic records. This discrepancy  
337 probably results from additional influences of other geodynamic processes, e.g., push force from  
338 the Reunion plume to the Indian Plate (Pusok and Stegman, 2020), which are excluded in the  
339 modelling. This poses a limitation in the present analysis. Addition of these factors might lead to  
340 convergence velocities significantly higher than present model values. However, such positive  
341 influences were perhaps countered by the presence of Indian continent, which would act as a sort  
342 of keel to reduce the plate velocity. Further model analyses are required to pinpoint their additional  
343 effects.

#### 4.1.2. *Cenozoic evolution of the Andaman System*

345 In the case of the Andaman Subduction System (Fig. 8a, b), the active subduction occurs  
346 currently at the northern flank of the Java trench where the oceanic part of the Indian Plate subducts  
347 at a low angle to the arc-trend beneath a small overriding-continental block (Fig. 5). This  
348 continental fragment, which is a detached part of the larger Indian Plate occurs parallel to the  
349 volcanic arc, forming the Andaman Island Chain. The Pliocene-Holocene volcanism in the inner  
350 arc of the Java Trench suggests that the subduction has remained active since the late Miocene

1  
2  
3  
4 351 (Acharyya et al., 1991; Sengupta et al., 1990). The Andaman Sea, a manifestation of extensional  
5  
6 352 tectonics and other similar basins in this region also opened up in the late Miocene (Curry, 2005).  
7  
8  
9 353 The Andaman Ophiolites occur in a flat-lying arrangement, showing a close spatial association  
10  
11  
12 354 with a zone of negative gravity anomalies that suggest their occurrence as thin sub-horizontal



13  
14  
15  
16  
17  
18  
19  
20  
21  
22  
23  
24  
25  
26  
27  
28  
29  
30 Figure 8: a) Bathymetric map of the Andaman Subduction Zone b) 3D block diagram of important  
31 components in the present-day Andaman–Nicobar subduction system along the BB' profile showing  
32 slab geometries and spatial relation between the two subduction systems and the Andaman micro-  
33 continent. c) Time snapshot (15 Myr) of the oceanic-continent double subduction model which  
34 simulates the last 30 Myr evolution of this eastern Neo-Tethyan region.

35  
36 355 bodies. Moreover, the ophiolite suits range in age between late Mesozoic and early Eocene, much  
37  
38 356 older than the Andaman Sea crust. These observations indicate that the Andaman and other related  
39  
40  
41 357 ophiolites farther north in this convergent zone were derived from a suture to the east during late  
42  
43 358 Oligocene time and emplaced as nappes during the middle Eocene. The geochronological order  
44  
45 359 indicates the existence of a second subduction zone at the time of late-Miocene subduction  
46  
47  
48 360 (continuing to present day) and opening of the Andaman Sea (Khan & Chakraborty, 2005). Our  
49  
50 361 micro-continent-oceanic plate model (Fig. 4) explains how the SDDS dynamics controlled such a  
51  
52 362 tectonic evolution in the Andaman convergent belt. The FSZ simulates the mid-Eocene subduction  
53  
54 363 event where the Indo-Australian oceanic lithosphere continued to subduct beneath the Burma Plate  
55  
56  
57 364 (equivalent to the stiffer OP in the model). The model setup produces an extensional spreading  
58  
59  
60  
61  
62  
63  
64  
65

1  
2  
3  
4  
5  
6  
7  
8  
9  
10  
11  
12  
13  
14  
15  
16  
17  
18  
19  
20  
21  
22  
23  
24  
25  
26  
27  
28  
29  
30  
31  
32  
33  
34  
35  
36  
37  
38  
39  
40  
41  
42  
43  
44  
45  
46  
47  
48  
49  
50  
51  
52  
53  
54  
55  
56  
57  
58  
59  
60  
61  
62  
63  
64  
65

365 centre as a consequence of some pre-existing lithospheric flaws, switching a remarkable change  
366 in the evolutionary course of the single-subduction system. The mechanical weakness might have  
367 developed due to the southward propagation of dextral motion in the Sagaing Fault System, which  
368 was active well before Miocene to set the mechanical conditions necessary for the Andaman Sea  
369 opening. The formation of this extensional zone eventually led to the late Miocene emergence of  
370 the Andaman Sea basin. The microcontinental fragment (*cf.* Andaman continental block)  
371 eventually decoupled itself from the ongoing subducting slab, and initiated a second subduction in  
372 the same region, as observed in our model at ~6 Myr (Fig. 8c). The newly formed subduction can  
373 be compared with the presently active Indo-Australian oceanic subduction below the Java Trench.  
374 The model suggests that both the subduction remained active for a considerable time (~24 Myr)  
375 and facilitated the Indo-Australian Plate motion relative to the Burma Plate. With time, the younger  
376 oceanic lithosphere formed at the Andaman Sea spreading centre drifted to the trench close to the  
377 Burma Plate and resulted in oceanic slab detachment as the lithosphere failed to gain density  
378 required for the mid-Eocene subduction.

#### 4.1.3. *Post-Cretaceous Indo-Eurasian Convergence*

380 The India-Eurasia convergence during the Cenozoic period had a collision between continental  
381 India and the Kohistan arc (Burg, 2011) and subsequently, with the Gangdese-Karakoram  
382 continental arc, resulting in the closure of the Neo-Tethyan basin. The opening of the Carlsberg  
383 Ridge in the Indian Ocean basin characterises the region south of the Indian continent (Fig 9c).  
384 The multiple continental plate model demonstrates the Cenozoic Indo-Eurasian collisional tectonic  
385 history very well. This model reproduces the collision of the Indian continental plate with the  
386 Eurasian Plate (~45 Ma) (Ding et al., 2005, 2016; Khan et al., 2009) when the oceanic subduction  
387 below Eurasia was active. Interestingly, the Carlsberg ridge had a fast spreading in late Cretaceous

(Merkouriev and Sotchevanova, 2003), which is found in our model that forms a spreading ridge and a second subduction in the ridge's vicinity. Based on our model results, we propose that the subduction occurred at the present-day position of the Amirante Trench- a trough-like feature,

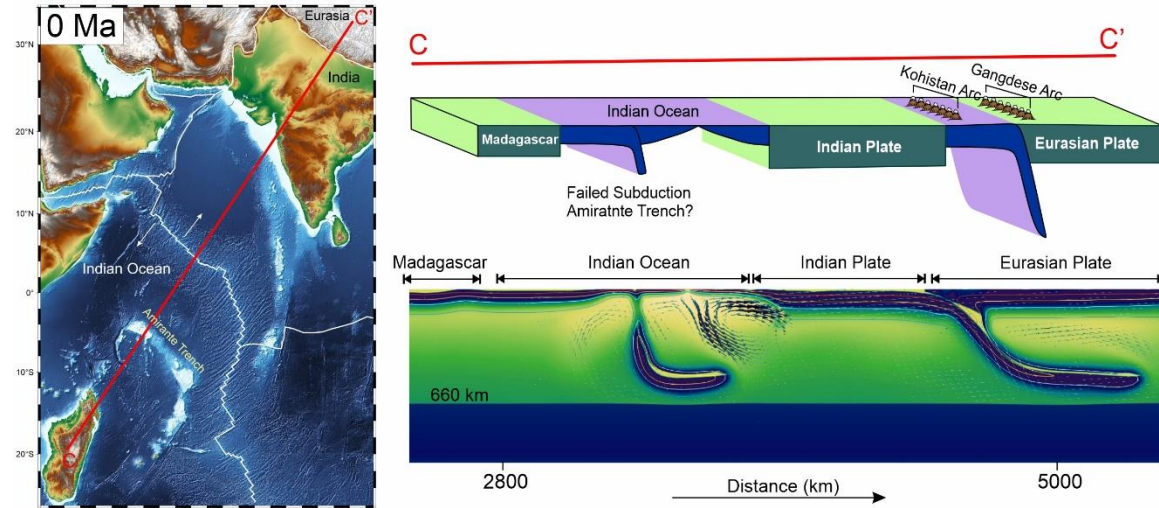


Figure 9: a) Bathymetric map of the Indo-Eurasian convergence zone and its related features b) Cross section along CC' showing slab geometries and distances between the prominent subduction features resulting in the convergence of the Indian plate with the Eurasian plate c) Time snapshot at 20 Myr of the multiple continent SDDS model which simulates the Post-Cretaceous evolution of the Indo-Eurasian collision zone.

approximately 600 km long in the western Indian Ocean (Fig. 9a). Geological and geophysical studies show evidence of partial or limited subduction within the trench (Miles, 1982). As observed in our model, the subduction was active in this region for ~4 Myr but ceased its activity following the slab detachment under the influence of a continental block (analogous to the Madagascar continental fragment in nature). The collision between the Indian and Eurasian continents led to a dramatic shift from retreating to advancing trench motion and a decrease in the Carlsberg ridge spreading rate, both of which are compatible with the model results. Our model results show that this tectonic system did not lead to the formation of a matured SDDS zones due to the influence of the continental blocks.

#### 4.2. Double-subduction evolution by feedback mechanisms

1  
2  
3  
4 401 The present model experiments demonstrate that a double-subduction system can grow  
5  
6 402 spontaneously from pre-existing weak zones (Bercovici and Ricard, 2014; Maunder et al., 2020)  
7  
8  
9 403 under slab-pull dynamics. The two subduction zones in such systems, however, evolve in a  
10  
11 404 competing mode, one suppressing the other, ultimately leading to their unequal development on a  
12  
13  
14 405 million-year timescale. To illustrate this, consider our double-subduction model for an oceanic  
15  
16 406 plate setting as applicable to the Trans-Tethyan System evolution during Cretaceous. The model  
17  
18  
19 407 shows synchronous initiation of subduction at two lithospheric weak zones (Rear and Fore  
20  
21 408 Subduction Zone: RSZ and FSZ), but one of them (RSZ) preferentially becomes the most active  
22  
23  
24 409 zone (subduction velocity:~11 cm/yr), suppressing the other slab (FSZ) motion to remain  
25  
26 410 significantly weak (~1.5 cm/yr). This competing double-subduction dynamics causes the second  
27  
28  
29 411 subduction to become more active once the first subducting slab encounters resistance at the lower  
30  
31 412 mantle at 660 km. The reduced slab motion, coupled with a trench retreat motion in one subduction  
32  
33  
34 413 has a feedback effect on the second subduction in accelerating slab motion (~1.5 to ~6 cm/yr). To  
35  
36 414 quantitatively evaluate the competing evolution of a double subduction system, we compare the  
37  
38 415 SDDS model results with those from a subduction model, containing a single subduction system  
39  
40  
41 416 equivalent to the FSZ (details provided in Supplementary S1). The model comparison reveals that  
42  
43 417 the RSZ activity significantly delays the FSZ initiation (~13.4 Myr), which, in contrast, begins to  
44  
45  
46 418 occur much quicker (3.4 Myr) in the single subduction model (Fig. S2). In addition, the FSZ  
47  
48 419 activity, in overall becomes significantly sluggish due to its interaction with the RSZ in the oceanic  
49  
50  
51 420 double subduction system.

52  
53 421 The other two model settings (Figs. 4,5) show similar feedback effects on the development  
54  
55 422 of double-subduction systems. In the microcontinent-bearing oceanic plate setting, analogous to  
56  
57  
58 423 that of Andaman subduction system, the double subduction processes operate almost equally (Fig.  
59  
60  
61  
62  
63  
64  
65



1  
2  
3  
4  
5  
6  
7  
8  
9  
10  
11  
12  
13  
14  
15  
16  
17  
18  
19  
20  
21  
22  
23  
24  
25  
26  
27  
28  
29  
30  
31  
32  
33  
34  
35  
36  
37  
38  
39  
40  
41  
42  
43  
44  
45  
46  
47  
48  
49  
50  
51  
52  
53  
54  
55  
56  
57  
58  
59  
60  
61  
62  
63  
64  
65

4) 424 forming a spreading centre between the two subduction zones. However, the new lithosphere  
425 formed in the spreading centre causes the frontal subduction zone (FSZ) to undergo slab  
426 detachment, which in turn facilitates the slab motion in the rear subduction zone (RSZ). The  
427 multiple continental plate setting also shows a time-dependent interaction between the RSZ and  
428 FSZ during their evolution. The FSZ slab motion hardly allows the RSZ to become significantly  
429 active until the slab encounters the lower mantle to slow down its motion. The RSZ slab starts to  
430 actively sink when the RSZ almost reaches the upper-lower mantle boundary after a time of ~11  
431 Myr. The feedback direction reverses as the RSZ experiences slab detachment due to resistance  
432 offered by the continent in the rear subducting oceanic plate. The paleo-trench at Amirante is an  
433 excellent example of subduction that failed to attain maturity due to the influence of the  
434 Madagascar continental plate. Thus, the model examples discussed here suggest that the SDDS  
435 systems generally evolve with a feedback relation between the two subduction zones that mutually  
436 interact with one another. To advance these findings, further studies are required to compare the  
437 model results with corresponding single-subduction model simulations and quantify the additional  
438 effects of slab-slab interaction in the SDDS systems.

### 4.3. *Influence of continental heterogeneities*

440 Previous studies have shown that the complexity in double-subduction systems, as compared  
441 to single-subduction settings, originates mainly from the effects of inter-slab interactions in plate  
442 bending, coupled with additional factors, contrasting plate ages, plate dimensions, rheology, and  
443 inter-slab distance (Mishin et al., 2008; Cížková & Bina 2015; Holt et al., 2017). This study  
444 identifies the presence of microcontinental blocks or continental plates in oceanic plate tectonic  
445 settings as an additional influential factor in the dynamics and stability of a double-subduction  
446 system. Microcontinents are mostly surrounded by oceanic crust, and they form by extension and

1  
2  
3  
4  
5  
6  
7  
8  
9  
10  
11  
12  
13  
14  
15  
16  
17  
18  
19  
20  
21  
22  
23  
24  
25  
26  
27  
28  
29  
30  
31  
32  
33  
34  
35  
36  
37  
38  
39  
40  
41  
42  
43  
44  
45  
46  
47  
48  
49  
50  
51  
52  
53  
54  
55  
56  
57  
58  
59  
60  
61  
62  
63  
64  
65

447 breakup of continental masses, followed by plate boundary relocations. Jan-Mayen in the north-  
448 east Atlantic Ocean (Gaina et al., 2009; Peron-Pinvidic et al., 2012), Andaman in the Indian Ocean  
449 (Bandyopadhyay et al., 2020) and several small, isolated islands around Australia (Gaina et al.,  
450 2003) are typical examples of microcontinents. Our microcontinent-oceanic double-subduction  
451 model suggests that such microcontinents play a vital role in localizing a spreading centre (location  
452 of new lithosphere generation) between the two subduction zones. The spreading centre, however,  
453 remains active for a specific time span, and its activity weakens following the slab detachment in  
454 the FSZ. This mechanism can be directly compared to the opening of the Andaman Sea extensional  
455 zone, synchronous to the initiation of the present-day subduction below the Andaman  
456 microcontinent.

457         The model results show that an oceanic plate setting in the absence of any continental blocks  
458 can readily form a double subduction system, initiated by pre-existing lithospheric weak zones in  
459 the plate setting. However, a buoyant continental fragment selectively prevents the subduction  
460 zones in front of this plate to mature with time, and forces the system to evolve unequally at the  
461 two trenches. Similarly, a multiple-continental assemblage reduces the convergence rates due to  
462 their buoyancy and continent-arc collision effects, described as *transference* by Stern (2004) to  
463 show the accretion-assisted continental growth mechanism. The reducing convergence rates result  
464 in tensile stresses in the subducting slab, eventually leading to slab detachment (Fig. 5). The model  
465 results suggest that microcontinental blocks can greatly influence the evolution of subduction  
466 processes, as reported from several natural subduction systems, such as the northern Luzon, the  
467 Puysegur (New Zealand) and the Andaman subduction zones (Bandyopadhyay et al., 2020; Zhu et  
468 al., 2023). The microcontinents provide a potential location of passive continental margin that  
469 transforms into a tectonically active region by subduction initiation as evident in the evolution

1  
2  
3  
4  
5  
6  
7  
8  
9  
10  
11  
12  
13  
14  
15  
16  
17  
18  
19  
20  
21  
22  
23  
24  
25  
26  
27  
28  
29  
30  
31  
32  
33  
34  
35  
36  
37  
38  
39  
40  
41  
42  
43  
44  
45  
46  
47  
48  
49  
50  
51  
52  
53  
54  
55  
56  
57  
58  
59  
60  
61  
62  
63  
64  
65

470 Andaman subduction system. Due to their lower mechanical strength, compared to that of large  
471 continental plates they localize subduction and facilitate the process to occur at faster rates.

472 *4.4. Subduction-driven spreading centres: location of new plate generation*

473 Generally, single-subduction systems involve slab rollback, which is often accommodated  
474 by horizontal extension and formation of a spreading centre (back-arc basin) in the overriding  
475 plate. Double-subduction systems in an oceanic plate setting, on the other hand, forces the rear  
476 trench to retreat at fast rates as the frontal plate moves in the opposite direction, offering less  
477 resistance to the rear slab. This kinematic state results in formation of a spreading centre at the rear  
478 trench, which eventually acts as a site for new lithosphere generation. This mechanism allows the  
479 RSZ to accommodate slab roll back without involving overriding plate kinematics, as in a single-  
480 subduction setting. This model study thus brings out the importance of such spontaneous spreading  
481 centre formation in the SDDS evolution within large oceanic plates.

482 Our modelling demonstrates that spreading centres crucially control the subduction  
483 dynamics in transforming a double- to a single-subduction system. The microcontinent-oceanic  
484 plate model shows the development of large tensile stresses in the region between the older  
485 subducting plate and the newly formed lithosphere at the trench, which causes the older slab to  
486 experience detachment. The slab break-off eventually stops the subduction activity, leaving the  
487 other subduction active. Spreading centres also play an important role in the onset of convergent  
488 setting and promotes decoupling in a large oceanic plate (e.g., *oceanic plate model*, Fig. 3). Such  
489 tectonic processes are observed in other natural systems, for example, the Cocos-Nazca spreading  
490 centre where the spreading centre formed by splitting of the oceanic lithosphere, giving rise to the  
491 Farallon plate break up in the early Miocene.

492

1  
2  
3  
4  
5  
6  
7  
8  
9  
10  
11  
12  
13  
14  
15  
16  
17  
18  
19  
20  
21  
22  
23  
24  
25  
26  
27  
28  
29  
30  
31  
32  
33  
34  
35  
36  
37  
38  
39  
40  
41  
42  
43  
44  
45  
46  
47  
48  
49  
50  
51  
52  
53  
54  
55  
56  
57  
58  
59  
60  
61  
62  
63  
64  
65

## 493 5. Conclusions

494 The key results of this research are two-fold: firstly, it unveils the intricate mechanisms governing  
495 the development of same-dip double subduction (SDDS) systems. Secondly, it provides new  
496 insights into the role of SDDS dynamics in the Neo-Tethyan tectonic evolution. The principal  
497 findings of this study are summarized as follows: 1) SDDS are initiated spontaneously in presence  
498 of lithospheric-scale mechanical weaknesses, e.g., faults, without any aid of kinematic  
499 perturbations, in contrary to that suggested in earlier studies. Throughout the temporal progression  
500 of a SDDS system, the two subducting slabs mutually affect their kinematics and subduction-  
501 driven flow patterns in the mantle wedges as well as asthenosphere. 2) SDDS systems can remain  
502 active for a long period of time (>25 Myr) in an oceanic setting, and eventually attain exceptionally  
503 high convergence velocities, 16-17 cm/year during its extended period (~5 Myr) of activity,  
504 depending on the slab ages at the trenches. These model findings explain the development of a  
505 self-sustaining SDDS responsible for the anomalously Indo-Eurasian high-convergence velocity  
506 condition in the Cretaceous Neo-Tethyan evolution. 3) The presence of continental blocks in the  
507 initial plate setting greatly influences the SDDS dynamics, forcing the double subduction zones to  
508 localize preferentially at their passive margins with the oceanic plates. They grow almost equally,  
509 forming a spreading centre between the two trenches on a time scale of 25 Myr. This SDDS model  
510 accounts for the Cenozoic tectonic evolution in the eastern Neo-Tethyan region, which ultimately  
511 formed the Andaman subduction system. 4) In an initial plate configuration with multiple  
512 continental fragments or plates, the latter can cause one of the SDDS slabs to halt its motion,  
513 resulting in a double to single-subduction transformation, which occurred in the Amirante-India-  
514 Eurasia subduction system during the Cenozoic evolution of Neo-Tethys.

1  
2  
3  
4  
5  
6  
7  
8  
9  
10  
11  
12  
13  
14  
15  
16  
17  
18  
19  
20  
21  
22  
23  
24  
25  
26  
27  
28  
29  
30  
31  
32  
33  
34  
35  
36  
37  
38  
39  
40  
41  
42  
43  
44  
45  
46  
47  
48  
49  
50  
51  
52  
53  
54  
55  
56  
57  
58  
59  
60  
61  
62  
63  
64  
65

516 **Declaration of Competing Interest**

517 The authors declare that they have no known competing financial interests or personal  
518 relationships that could have appeared to influence the work reported in this article.

519  
520 **Acknowledgments**

521 We thank two anonymous reviewers and Editor Carolina Lithgow-Bertelloni for their constructive  
522 suggestions and incisive comments, which have greatly improved our present study. The work has  
523 been performed under the Project HPC-EUROPA3 (INFRAIA-2016-1-730897), with the support  
524 of the EC Research Innovation Action under the H2020 Programme; in particular, A.R. gratefully  
525 acknowledges the support of Durham University and the computer resources and technical support  
526 provided by EPCC, University of Edinburgh. A.R. gratefully acknowledges CSIR, India for  
527 awarding research fellowship grants (09/096(0940)/2018- EMR-I). This work used the ARCHER2  
528 UK National Supercomputing Service (<https://www.archer2.ac.uk>). The DST-SERB is  
529 acknowledged for supporting this work through the J.C. Bose fellowship (JBR/2022/000003) to  
530 N.M.

531  
532 **Data Availability Statement**

533 The authors confirm that all the data used to support the findings of this study are available within  
534 the article and as supplementary materials. All aspects of UNDERWORLD 2 (Mansour, J., et al.,  
535 2020) can be checked here (<https://doi.org/10.5281/zenodo.6820562>).

Description	Symbol	Unit	Default Values
-------------	--------	------	----------------

1  
2  
3  
4  
5  
6  
7  
8  
9  
10  
11  
12  
13  
14  
15  
16  
17  
18  
19  
20  
21  
22  
23  
24  
25  
26  
27  
28  
29  
30  
31  
32  
33  
34  
35  
36  
37  
38  
39  
40  
41  
42  
43  
44  
45  
46  
47  
48  
49  
50  
51  
52  
53  
54  
55  
56  
57  
58  
59  
60  
61  
62  
63  
64  
65

Thermal expansion coefficient	$\alpha$	$\text{K}^{-1}$	$3 \times 10^5$
Thermal diffusivity	$\kappa$	$\text{m}^2 \text{s}^{-1}$	$10^{-6}$
Reference density	$\rho_0$	$\text{kg m}^{-3}$	3300
Surface temperature	$T_s$	K	273
Potential temperature	$T_m$	K	1673
Adiabatic temperature gradient	$dT/dz$	$\text{K km}^{-1}$	0.37
Gravitational acceleration	$g$	$\text{m s}^{-2}$	9.81
Maximum viscosity	$\eta_{max}$	Pa s	$1.0 \times 10^{24}$
Minimum viscosity	$\eta_{min}$	Pa s	$1.0 \times 10^{19}$
Crust viscosity	$\eta_c$	Pa s	$1.0 \times 10^{20}$
<b>Dislocation creep (Upper Mantle)</b>			
Activation energy	$E$	$\text{kJ mol}^{-1}$	540
Activation volume	$V$	$\text{cm}^3 \text{mol}^{-1}$	10
Pre-factor	$A$	$\text{Pa}^n \text{s}^{-1}$	$4.1 \times 10^{15}$
Exponent	$n$	-	3.5
<b>Diffusion creep (Upper and Lower mantle)</b>			
Activation energy	$E$	$\text{kJ mol}^{-1}$	300 (UM & LM)
Activation volume	$V$	$\text{cm}^3 \text{mol}^{-1}$	4.5 (UM), 1.58 (LM)
Pre-factor	$A$	$\text{Pa}^1 \text{s}^{-1}$	$1.87 \times 10^9$ (UM) $1.77 \times 10^{14}$ (LM)
Exponent	$n$	-	1

<b>Plastic yielding</b>			
Cohesion	$C_0$	MPa	20
Friction coefficient	$\mu$	-	0.1
Maximum yield stress	$\tau_{max}$	MPa	500

Table 1: List of model parameters and their corresponding values chosen for the numerical simulations.

## 6. Appendix A

### 6.1 Governing equations

We build numerical, time-evolving, dynamically consistent thermomechanical subduction models in 2-D Cartesian domains within a theoretical framework of computational fluid dynamics (CFD), implemented by using the UNDERWORLD2 code (Mansour et al., 2020). This CFD simulation study assumes an incompressible Boussinesq fluid flow, approximated to the long-time (multi-million year) scale kinematic state of Earth’s mantle. This approximation accounts for only buoyancy (body force term), treating all other effects of density fluctuations negligibly small in the momentum equation. We use the continuity and momentum conservation equations in our modelling to describe spontaneous flows in our model driven by density anomalies. The expressions of these equations are, respectively,

$$\frac{\delta u_i}{\delta x_i} = 0 \quad (1)$$

$$-\frac{\delta P}{\delta x_i} + \frac{\delta \sigma_{ij}}{\delta x_j} + \rho g_i = 0 \quad (2)$$

1  
2  
3  
4 550 where  $v_i$  is the velocity vector. In Eq. (2) the inertial forces are neglected, as applicable to long  
5  
6  
7 551 term flows in the mantle.  $\sigma_{ij}$  can be decomposed into the isotropic ( $\sigma^o_{ij}$ ) and the deviatoric stress  
8  
9 552 ( $\tau_{ij}$ ) tensors as,

$$\sigma_{ij} = \sigma^o_{ij} + \tau_{ij} \quad (3)$$

11  
12  
13  
14  
15  
16 553 such that

$$\sigma^o_{ij} = P\delta_{ij} \quad (4)$$

$$\tau_{ij} = 2\eta\dot{\epsilon}_{ij} = \eta\left(\frac{\partial u_i}{\partial x_j} + \frac{\partial u_j}{\partial x_i}\right) \quad (5)$$

26 554 where  $\dot{\epsilon}_{ij}$  is the strain rate tensor. Substituting Eq. (4) & (5) into Eq. (2) gives rise to the Stokes  
27  
28  
29 555 equation with pressure and velocity as two unknown variable parameters. Applying the model  
30  
31 556 boundary conditions, we numerically solve the continuity and Stokes equations in a pre-defined  
32  
33  
34 557 2D Cartesian domain to derive the velocity and pressure in the model domain.

35  
36 558 The thermal evolution of a subduction system is dictated by combined effects of advective heat  
37  
38  
39 559 transfer, thermal diffusion, and heat sources/sinks within the system, which we tackle with the  
40  
41 560 following heat equation.

$$\rho C_p \frac{DT}{Dt} = \frac{\partial q_i}{\partial x_i} + \rho Q, \quad (6)$$

42  
43  
44  
45  
46  
47  
48 561 where  $Q$  is the rate of internal heat production per unit volume,  $T$  is the temperature,  $\rho$  is the  
49  
50  
51 562 material density and  $C_p$  is the specific heat.  $q$  represents the rate of diffusional heat transfer,  
52  
53 563 described by Fourier's law as,

$$q_i = -k \frac{\partial T'}{\partial x_i}, \quad (7)$$

54  
55  
56  
57  
58  
59  
60  
61  
62  
63  
64  
65



1  
2  
3  
4 564 where  $k$  is the thermal conductivity and  $T'$  is the nonadiabatic temperature. Substituting Eq. (7)  
5  
6  
7 565 into (6) and expanding considering the definition of material derivative, gives

$$\frac{\partial T}{\partial t} + u_i \frac{\partial T'}{\partial x_i} = \kappa \nabla^2 T' + \frac{Q}{C_p} \quad (8)$$

10  
11  
12  
13  
14 566 where  $\kappa = \frac{k}{\rho C_p}$ , which represents the thermal diffusivity.  $T'$  is replaced by the adiabatic  
15  
16  
17  
18 567 temperature ( $T_a$ ) of the system as a function of depth ( $z$ ) obtained from the relation:

$$T_a = T' + z \left( \frac{\partial T'}{\partial z} \right) = T' + z \left( \frac{\alpha g T_p}{C_p} \right), \quad (9)$$

20  
21  
22  
23  
24  
25 568 where  $T_p$  is the mantle potential temperature and  $\alpha$  is the coefficient of thermal expansion, which  
26  
27  
28 569 was set at a value of  $3 \times 10^{-5} \text{ K}^{-1}$ . Considering  $C_p = 1260 \text{ J/kg/K}$  for Earth's mantle, a resultant  
29  
30  
31 570 adiabatic temperature gradient of  $0.4 \text{ K/km}$  is added to the nonadiabatic temperature of the mantle.  
32  
33 571 The energy conservation equation (8) is solved using the Semi-Lagrangian Crank-Nicholson  
34  
35 572 (SLCN) method (Spiegelman and Katz, 2006), built upon the potencies of the Crank-Nicolson  
36  
37  
38 573 scheme for diffusion and the semi-Lagrangian scheme for advection. The SLCN method has been  
39  
40 574 found to be unconditionally stable, allowing large time-step sizes. We impose constant (Dirichlet)  
41  
42  
43 575 and zero-flux (Neumann) on the top and bottom boundaries, respectively to solve the energy  
44  
45 576 equation. The model surface temperature is set initially at  $0^\circ\text{C}$ , whereas the initial model basal  
46  
47  
48 577 temperature at  $1800^\circ\text{C}$ .

49  
50 578 We use half-space cooling profiles to constrain the thermal structures of model lithospheric  
51  
52 579 plates corresponding to their assigned ages, considering a thermal diffusivity value of  $10^{-6} \text{ m}^2/\text{s}$   
53  
54  
55 580 (van Hunen and Allen, 2011), and a mantle potential temperature of  $1400^\circ \text{C}$  (Holt and Condit,  
56  
57 581 2021). The model density parameters are chosen as a function of the assigned temperatures, taking  
58  
59  
60  
61  
62  
63  
64  
65

1  
2  
3  
4 582 into account the thermal properties and their evolution following the momentum equation. For  
5  
6  
7 583 temperature dependent density variations, we adopt the equation of state,

$$\rho = \rho_r(1 - \alpha(T - T_p)) \quad (10)$$

10  
11  
12  
13 584 where  $\rho_r$  denotes the reference mantle density at the mantle potential temperature, which is set at  
14  
15 585 3300 kg/m<sup>3</sup>.

## 18 586 6.2. Rheological considerations

20  
21 587 We model the mantle rheology in the framework of a composite creep law that combines  
22  
23 588 diffusion creep ( $\eta_{diff}$ ), dislocation creep ( $\eta_{disl}$ ), and plastic yielding ( $\eta_{yield}$ ). An Arrhenius  
24  
25  
26 589 temperature and pressure dependence of the activation volume ( $V$ ) and the activation energy ( $E$ )  
27  
28 590 (Hirth and Kohlstedt, 2004) is chosen to describe the creep laws for mantle silicates, which leads  
29  
30  
31 591 to the diffusion/dislocation-controlled viscosity,

$$\eta_{diff/disl} = A \frac{-1}{n} \dot{\epsilon}^{\frac{1-n}{n}} \exp\left(\frac{E + P_1 V}{nRT_a}\right) \quad (11)$$

32  
33  
34  
35  
36  
37  
38 592 where  $A$  is a pre-factor,  $n$  is the stress exponent ( $n = 1$  and  $3.5$  for diffusional and dislocation creep,  
39  
40 593 respectively),  $R$  is the gas constant and  $P_1$  is the lithostatic pressure. It is usually observed that  
41  
42  
43 594 lithostatic pressure enhances the yield strength of mantle material by different stress-limiting  
44  
45 595 mechanisms. In contrast, material strength can be reduced as a consequence of brittle yielding  
46  
47  
48 596 (Kohlstedt et al., 1995) near the surface. These two yield mechanisms are combined into a  
49  
50 597 simplified plastic rheology (van Hunen and Allen, 2011), and the viscosity is described as,

$$\eta_{yield} = \frac{\tau_{yield}}{2\dot{\epsilon}} \quad (12)$$

52  
53  
54  
55  
56  
57 598 and  $\tau_{yield}$  denotes the yield strength, expressed by the following relation.  
58  
59  
60  
61  
62  
63  
64  
65

$$\tau_{yield} = \min ( C + \mu P, \tau_{max} ) \quad (13)$$

599 where  $C$  (= 20 MPa) is the initial cohesion,  $\mu$  (= 0.1) is the friction coefficient, and  $\tau_{max}$  is the cut-  
600 off yield stress value. The harmonic mean of the three types of viscosity is considered to determine  
601 an effective model viscosity ( $\eta_{eff}$ ),

$$\frac{1}{\eta_{eff}} = \frac{1}{\eta_{diff}} + \frac{1}{\eta_{disl}} + \frac{1}{\eta_{yield}} \quad (14)$$

602 The activation volumes ( $V$ ) and energies ( $E$ ) values (Table 1) chosen in our modelling are  
603 consistent with the experimental estimates for dry olivine (Karato and Wu, 1993). We have  
604 considered the value of pre- factor  $A$  for the upper mantle based on the following findings, 1) an  
605 effective viscosity in the order of  $10^{20}$  Pa in the shallow part of upper mantle (Hager, 1990), and  
606 2) seismic anisotropy implying dominantly dislocation creep in the majority part of mantle  
607 (Becker, 2006). Diffusional creep is recognized as the principal mechanism to determine the lower-  
608 mantle rheology (Karato & Wu, 1993). A range of estimates suggest its viscosity significantly  
609 higher than the upper-mantle viscosity. The calculated creep pre-factor yields a value of  $3 \times 10^{22}$   
610 at the 660 km transition (Čížková et al., 2012), which increases continuously with depth (Fig. 2).

611 The top crustal layer in our model is assigned a constant viscosity of  $1 \times 10^{20}$  Pa s. We use  
612 Eq. (12) to simulate brittle failure in this layer, assuming a low value (10 MPa) of its cohesion.  
613 This rheological consideration aims to reproduce the mode crust with yield strength lower than  
614 that of the lithosphere. This modelling manipulation allows us to introduce decoupling of the  
615 subducting slab from the overriding plate and facilitate the plate convergence process. The mantle  
616 lithosphere strength is determined from the upper viscosity cut-off values ( $1 \times 10^{24}$  Pa s), except  
617 for regions where we preferentially activate plastic yielding. For the overriding plate (OP), the  
618 upper limit of viscosity is increased to  $2.5 \times 10^{24}$  Pa s to obtain a slightly higher stiffness. We

1  
2  
3  
4  
5  
6  
7  
8  
9  
10  
11  
12  
13  
14  
15  
16  
17  
18  
19  
20  
21  
22  
23  
24  
25  
26  
27  
28  
29  
30  
31  
32  
33  
34  
35  
36  
37  
38  
39  
40  
41  
42  
43  
44  
45  
46  
47  
48  
49  
50  
51  
52  
53  
54  
55  
56  
57  
58  
59  
60  
61  
62  
63  
64  
65

619 model the crust and the lithosphere individually single layers without any internal rheological  
620 stratification. Considering the long-term process of our present concern, the effects of elastic  
621 deformation are completely excluded. We add passive tracers in the compositional field within the  
622 regions of interest to track the plate motion and deformation during the model run.

### 6.3. Model Setup

We meshed the 2D domain by smaller quadrilateral elements with a mesh resolution of 512  
elements in the vertical direction, which provides an element width of  $\sim 2$  km, and a particle density  
of 50 tracers per element. These Lagrangian tracer particles used to track advecting materials and  
their corresponding physical properties are mapped to quadrature points with nearest-neighbour  
interpolation (Sandiford and Moresi, 2019). All models were subjected to  $g = 9.8 \text{ m/s}^2$ , where  $g$  is  
the acceleration due to gravity. The model has free-slip ( $v_y = 0$ ) conditions assigned to the bottom  
and top boundaries, whereas periodic boundary condition is imposed on the sidewalls.

For the temperature boundary condition, we impose constant (Dirichlet) and zero-flux  
(Neumann) on the top and bottom boundaries, respectively to solve the energy equation. We use  
half-space cooling profiles to constrain the thermal structures of model lithospheric plates  
corresponding to their assigned ages, considering a thermal diffusivity value of  $10^{-6} \text{ m}^2/\text{s}$  (van  
Hunen & Allen, 2011), and a mantle potential temperature of  $1400^\circ \text{ C}$  (Holt & Condit, 2021). The  
model density parameters are chosen as a function of the assigned temperatures, taking into  
account the thermal properties and their evolution following the momentum equation.

### 6.4. Numerical Scaling, Mesh Refinement Tests and Model validation

The governing equations (Section 6.1) and physical parameters are non-dimensionalized to  
implement them for the model simulations utilizing the UNDERWORLD2 scaling module. The  
model results, corresponding to the reference values of model parameters, are then scaled to their

1  
2  
3  
4  
5  
6  
7  
8  
9  
10  
11  
12  
13  
14  
15  
16  
17  
18  
19  
20  
21  
22  
23  
24  
25  
26  
27  
28  
29  
30  
31  
32  
33  
34  
35  
36  
37  
38  
39  
40  
41  
42  
43  
44  
45  
46  
47  
48  
49  
50  
51  
52  
53  
54  
55  
56  
57  
58  
59  
60  
61  
62  
63  
64  
65

642 equivalent real physical units. The scaling coefficients derived from the base units of length ( $Kl$ ),  
643 mass ( $Km$ ), time ( $Kt$ ) and temperature ( $KT$ ) are set as,  $Kl = 1$ ,  $Km = \rho_{ref} \times Kl^3$ ,  $Kt = 1 / (\frac{\eta_{ref} \times Kl}{Km})$   
644 and  $KT = T_p$ , where  $\rho_{ref}$  and  $\eta_{ref}$  are the reference density and viscosity, respectively. The scaling  
645 strategy has been implemented to keep buoyancy force as the sole driving factor in subduction of  
646 an oceanic lithosphere, assigned a non-dimensional value of 1 to aid the solver efficiency.

647 We kept a mesh resolution of  $1150 \times 512$  elements in our modelling. A set of resolution tests  
648 was performed for low ( $576 \times 256$ ,  $288 \times 128$  elements) as well as for a much higher resolution  
649 ( $2300 \times 1024$  elements), with an objective to optimize the refined resolution appropriate for  
650 subduction initiation modelling and tracking the evolutionary stages of a double subduction system  
651 with thin, weak viscoplastic subduction interfaces, and a composite rheology of the upper mantle.  
652 The mesh resolutions and their effects on the trench and subducting plate (SP) velocities are  
653 detailed in the Supplementary Section S4.

654  
655  
656  
657  
658  
659  
660  
661  
662  
663  
664

1  
2  
3  
4 **665 References:**  
5  
6

- 7 666 Acharyya, S.K., Ray, K.K., Sengupta, S., 1991. The Naga Hills and Andaman ophiolite belt, their  
8 667 setting, nature and collisional emplacement history. *Physics and Chemistry of the Earth* 18,  
9 668 293–315. [https://doi.org/10.1016/0079-1946\(91\)90006-2](https://doi.org/10.1016/0079-1946(91)90006-2)  
10 669 Advokaat, E.L., Bongers, M.L.M., Rudyawan, A., BouDagher-Fadel, M.K., Langereis, C.G., van  
11 670 Hinsbergen, D.J.J., 2018. Early Cretaceous origin of the Woyla Arc (Sumatra, Indonesia) on  
12 671 the Australian plate. *Earth Planet Sci Lett* 498, 348–361.  
13 672 <https://doi.org/10.1016/J.EPSL.2018.07.001>  
14 673 Aitchison, J.C., Badengzhu, Davis, A.M., Liu, J., Luo, H., Malpas, J.G., McDermid, I.R.C., Wu,  
15 674 H., Ziabrev, S. V., Zhou, M. fu, 2000. Remnants of a Cretaceous intra-oceanic subduction  
16 675 system within the Yarlung–Zangbo suture (southern Tibet). *Earth Planet Sci Lett* 183, 231–  
17 676 244. [https://doi.org/10.1016/S0012-821X\(00\)00287-9](https://doi.org/10.1016/S0012-821X(00)00287-9)  
18 677 Arcay, D., Lallemand, S., Abecassis, S., Garel, F., 2020. Can subduction initiation at a transform  
19 678 fault be spontaneous? *Solid Earth* 11, 37–62. <https://doi.org/10.5194/SE-11-37-2020>  
20 679 Auzemery, A., Willingshofer, E., Yamato, P., Duretz, T., Sokoutis, D., 2020. Strain localization  
21 680 mechanisms for subduction initiation at passive margins. *Glob Planet Change* 195, 103323.  
22 681 <https://doi.org/10.1016/J.GLOPLACHA.2020.103323>  
23 682 Bandyopadhyay, D., van Hinsbergen, D.J.J., Plunder, A., Bandopadhyay, P.C., Advokaat, E.,  
24 683 Chattopadhyaya, S., Morishita, T., Ghosh, B., 2020. Andaman Ophiolite: An Overview 1–17.  
25 684 [https://doi.org/10.1007/978-3-030-39843-9\\_1](https://doi.org/10.1007/978-3-030-39843-9_1)  
26 685 Becker, T.W., 2006. On the effect of temperature and strain-rate dependent viscosity on global  
27 686 mantle flow, net rotation, and plate-driving forces. *Geophys J Int* 167, 943–957.  
28 687 [https://doi.org/10.1111/J.1365-246X.2006.03172.X/2/M\\_167-2-943-EQ018.JPEG](https://doi.org/10.1111/J.1365-246X.2006.03172.X/2/M_167-2-943-EQ018.JPEG)  
29 688 Bercovici, D., Ricard, Y., 2014. Plate tectonics, damage and inheritance. *Nature* 2014 508:7497  
30 689 508, 513–516. <https://doi.org/10.1038/nature13072>  
31 690 Bouilhol, P., Jagoutz, O., Hanchar, J.M., Dudas, F.O., 2013. Dating the India–Eurasia collision  
32 691 through arc magmatic records. *Earth Planet Sci Lett* 366, 163–175.  
33 692 <https://doi.org/10.1016/J.EPSL.2013.01.023>  
34 693 Burg, J.P., 2011. The asia-kohistan-india collision: Review and discussion. *Frontiers in Earth*  
35 694 *Sciences* 4, 279–309. [https://doi.org/10.1007/978-3-540-88558-0\\_10/COVER](https://doi.org/10.1007/978-3-540-88558-0_10/COVER)  
36 695 Cande, S.C., Stegman, D.R., 2011. Indian and African plate motions driven by the push force of  
37 696 the Réunion plume head. *Nature* 2011 475:7354 475, 47–52.  
38 697 <https://doi.org/10.1038/nature10174>  
39 698 Čížková, H., Bina, C.R., 2015. Geodynamics of trench advance: Insights from a Philippine-Sea-  
40 699 style geometry. *Earth Planet Sci Lett* 430, 408–415.  
41 700 <https://doi.org/10.1016/J.EPSL.2015.07.004>  
42 701 Čížková, H., van den Berg, A.P., Spakman, W., Matyska, C., 2012. The viscosity of Earth’s lower  
43 702 mantle inferred from sinking speed of subducted lithosphere. *Physics of the Earth and*  
44 703 *Planetary Interiors* 200–201, 56–62. <https://doi.org/10.1016/J.PEPI.2012.02.010>  
45 704 Copley, A., Avouac, J.P., Royer, J.Y., 2010. India-Asia collision and the Cenozoic slowdown of  
46 705 the Indian plate: Implications for the forces driving plate motions. *J Geophys Res Solid*  
47 706 *Earth* 115, 3410. <https://doi.org/10.1029/2009JB006634>  
48 707 Corbi, F., Herrendörfer, R., Funicello, F., van Dinther, Y., 2017. Controls of seismogenic zone  
49 708 width and subduction velocity on interplate seismicity: Insights from analog and numerical  
50 709 models. *Geophys Res Lett* 44, 6082–6091. <https://doi.org/10.1002/2016GL072415>  
51  
52  
53  
54  
55  
56  
57  
58  
59  
60  
61  
62  
63  
64  
65

1  
2  
3  
4  
5  
6  
7  
8  
9  
10  
11  
12  
13  
14  
15  
16  
17  
18  
19  
20  
21  
22  
23  
24  
25  
26  
27  
28  
29  
30  
31  
32  
33  
34  
35  
36  
37  
38  
39  
40  
41  
42  
43  
44  
45  
46  
47  
48  
49  
50  
51  
52  
53  
54  
55  
56  
57  
58  
59  
60  
61  
62  
63  
64  
65

Curry, J.R., 2005. Tectonics and history of the Andaman Sea region. *J Asian Earth Sci* 25, 187–232. <https://doi.org/10.1016/J.JSEAES.2004.09.001>

Dasgupta, R., Mandal, N., 2018. Surface topography of the overriding plates in bi-vergent subduction systems: A mechanical model. *Tectonophysics* 746, 280–295. <https://doi.org/10.1016/J.TECTO.2017.08.008>

Ding, L., Kapp, P., Wan, X., 2005. Paleocene–Eocene record of ophiolite obduction and initial India-Asia collision, south central Tibet. *Tectonics* 24, 1–18. <https://doi.org/10.1029/2004TC001729>

Ding, L., Qasim, M., Jadoon, I.A.K., Khan, M.A., Xu, Q., Cai, F., Wang, H., Baral, U., Yue, Y., 2016. The India–Asia collision in north Pakistan: Insight from the U–Pb detrital zircon provenance of Cenozoic foreland basin. *Earth Planet Sci Lett* 455, 49–61. <https://doi.org/10.1016/J.EPSL.2016.09.003>

Eyuboglu, Y., Dudas, F.O., Zhu, D.C., Liu, Z., Chatterjee, N., 2019. Late Cretaceous I- and A-type magmas in eastern Turkey: Magmatic response to double-sided subduction of Paleo- and Neo-Tethyan lithospheres. *Lithos* 326–327, 39–70. <https://doi.org/10.1016/J.LITHOS.2018.12.017>

Faccenna, C., Holt, A.F., Becker, T.W., Lallemand, S., Royden, L.H., 2018. Dynamics of the Ryukyu/Izu-Bonin-Marianas double subduction system. *Tectonophysics* 746, 229–238. <https://doi.org/10.1016/J.TECTO.2017.08.011>

Gaina, C., Gernigon, L., Ball, P., 2009. Palaeocene-Recent plate boundaries in the NE Atlantic and the formation of the Jan Mayen microcontinent. *J Geol Soc London* 166, 601–616. <https://doi.org/10.1144/0016-76492008-112/ASSET/666CE50E-4E50-4EA4-825A-5FD0D19C5F10/ASSETS/GRAPHIC/601FIG10.JPEG>

Gaina, C., Müller, R.D., Brown, B., Ishihara, T., 2003. Microcontinent formation around Australia. *Special Paper of the Geological Society of America* 372, 405–416. <https://doi.org/10.1130/0-8137-2372-8.405>

Ghosh, B., Bandyopadhyay, D., Morishita, T., 2017. Andaman-Nicobar Ophiolites, India: Origin, evolution and emplacement. *Geological Society Memoir* 47, 95–110. <https://doi.org/10.1144/M47.7/ASSET/B51D4277-1DC1-4B58-A0F0-AA65A51742BC/ASSETS/IMAGES/LARGE/M47-1018F08.JPG>

Gürer, D., van Hinsbergen, D.J.J., Matenco, L., Corfu, F., Cascella, A., 2016. Kinematics of a former oceanic plate of the Neotethys revealed by deformation in the Ulukışla basin (Turkey). *Tectonics* 35, 2385–2416. <https://doi.org/10.1002/2016TC004206>

Hager, B.H., 1990. Mantle viscosity: a comparison of models from postglacial rebound and from the geoid, plate driving forces, and advected heat flux. *Glacial isostasy, sea-level and mantle rheology* 493–513. [https://doi.org/10.1007/978-94-011-3374-6\\_23/COVER](https://doi.org/10.1007/978-94-011-3374-6_23/COVER)

Hall, R., 2012. Late Jurassic–Cenozoic reconstructions of the Indonesian region and the Indian Ocean. *Tectonophysics* 570–571, 1–41. <https://doi.org/10.1016/J.TECTO.2012.04.021>

Hall, R., Spakman, W., 2002. Subducted slabs beneath the eastern Indonesia–Tonga region: insights from tomography. *Earth Planet Sci Lett* 201, 321–336. [https://doi.org/10.1016/S0012-821X\(02\)00705-7](https://doi.org/10.1016/S0012-821X(02)00705-7)

Heidbach, O., Reinecker, J., Tingay, M., Müller, B., Sperner, B., Fuchs, K., Wenzel, F., 2007. Plate boundary forces are not enough: Second- and third-order stress patterns highlighted in the World Stress Map database. *Tectonics* 26. <https://doi.org/10.1029/2007TC002133>

1  
2  
3  
4  
5  
6  
7  
8  
9  
10  
11  
12  
13  
14  
15  
16  
17  
18  
19  
20  
21  
22  
23  
24  
25  
26  
27  
28  
29  
30  
31  
32  
33  
34  
35  
36  
37  
38  
39  
40  
41  
42  
43  
44  
45  
46  
47  
48  
49  
50  
51  
52  
53  
54  
55  
56  
57  
58  
59  
60  
61  
62  
63  
64  
65

Hirth, G., Kohlstedt, D., 2004. Rheology of the Upper Mantle and the Mantle Wedge: A View from the Experimentalists. *Geophysical Monograph Series* 138, 83–105. <https://doi.org/10.1029/138GM06>

Holt, A.F., Condit, C.B., 2021. Slab Temperature Evolution Over the Lifetime of a Subduction Zone. *Geochemistry, Geophysics, Geosystems* 22, e2020GC009476. <https://doi.org/10.1029/2020GC009476>

Holt, A.F., Royden, L.H., Becker, T.W., 2017. The dynamics of double slab subduction. *Geophys J Int* 209, 250–265. <https://doi.org/10.1093/GJI/GGW496>

Jagoutz, O., Royden, L., Holt, A.F., Becker, T.W., 2015. Anomalously fast convergence of India and Eurasia caused by double subduction. *Nature Geoscience* 2014 8:6 8, 475–478. <https://doi.org/10.1038/ngeo2418>

Jolivet, L., Faccenna, C., Becker, T., Tesauro, M., Sternai, P., Bouilhol, P., 2018. Mantle Flow and Deforming Continents: From India-Asia Convergence to Pacific Subduction. *Tectonics* 37, 2887–2914. <https://doi.org/10.1029/2018TC005036>

Karato, S.I., Wu, P., 1993. Rheology of the Upper Mantle: A Synthesis. *Science* (1979) 260, 771–778. <https://doi.org/10.1126/SCIENCE.260.5109.771>

Khan, P.K., Chakraborty, P.P., 2005. Two-phase opening of Andaman Sea: a new seismotectonic insight. *Earth Planet Sci Lett* 229, 259–271. <https://doi.org/10.1016/J.EPSL.2004.11.010>

Király, Á., Funicello, F., Capitanio, F.A., Faccenna, C., 2021. Dynamic interactions between subduction zones. *Glob Planet Change* 202, 103501. <https://doi.org/10.1016/J.GLOPLACHA.2021.103501>

Király, Á., Holt, A.F., Funicello, F., Faccenna, C., Capitanio, F.A., 2018. Modeling Slab-Slab Interactions: Dynamics of Outward Dipping Double-Sided Subduction Systems. *Geochemistry, Geophysics, Geosystems* 19, 693–714. <https://doi.org/10.1002/2017GC007199>

Kohlstedt, D.L., Evans, B., Mackwell, S.J., 1995. Strength of the lithosphere: Constraints imposed by laboratory experiments. *J Geophys Res Solid Earth* 100, 17587–17602. <https://doi.org/10.1029/95JB01460>

Kufner, S.K., Schurr, B., Sippl, C., Yuan, X., Ratschbacher, L., Akbar, A. s/of M., Ischuk, A., Murodkulov, S., Schneider, F., Mechie, J., Tilmann, F., 2016. Deep India meets deep Asia: Lithospheric indentation, delamination and break-off under Pamir and Hindu Kush (Central Asia). *Earth Planet Sci Lett* 435, 171–184. <https://doi.org/10.1016/J.EPSL.2015.11.046>

Lamb, S., 2015. Kinematics to dynamics in the New Zealand Plate boundary zone: implications for the strength of the lithosphere. *Geophys J Int* 201, 552–573. <https://doi.org/10.1093/GJI/GGV027>

Lin, S.C., Kuo, B.Y., 2016. Dynamics of the opposite-verging subduction zones in the Taiwan region: Insights from numerical models. *J Geophys Res Solid Earth* 121, 2174–2192. <https://doi.org/10.1002/2015JB012784>

Maiti, G., Roy, A., Sen, J., Mandal, N., 2021. Impact of Decelerating India-Asia Convergence on the Crustal Flow Kinematics in Tibet: An Insight From Scaled Laboratory Modeling. *Geochemistry, Geophysics, Geosystems* 22, e2021GC009967. <https://doi.org/10.1029/2021GC009967>

Mansour, J., Giordani, J., Moresi, L., Beucher, R., Kaluza, O., Velic, M., Farrington, R., Quenette, S., Beall, A., 2020. Underworld2: Python Geodynamics Modelling for Desktop, HPC and Cloud. *J Open Source Softw* 5, 1797. <https://doi.org/10.21105/joss.01797>



1  
2  
3  
4  
5  
6  
7  
8  
9  
10  
11  
12  
13  
14  
15  
16  
17  
18  
19  
20  
21  
22  
23  
24  
25  
26  
27  
28  
29  
30  
31  
32  
33  
34  
35  
36  
37  
38  
39  
40  
41  
42  
43  
44  
45  
46  
47  
48  
49  
50  
51  
52  
53  
54  
55  
56  
57  
58  
59  
60  
61  
62  
63  
64  
65

Maunder, B., Prytulak, J., Goes, S., Reagan, M., 2020. Rapid subduction initiation and magmatism in the Western Pacific driven by internal vertical forces. *Nature Communications* 2020 11:1 11, 1–8. <https://doi.org/10.1038/s41467-020-15737-4>

Merkouriev, S.A., Sotchevanova, N.A., 2003. Structure and evolution of the Carlsberg Ridge: Evidence for non-stationary spreading on old and modern spreading centres on JSTOR [WWW Document]. *Curr Sci*. URL <https://www.jstor.org/stable/24108663> (accessed 11.8.23).

Miles, P.R., 1982. Gravity models of the Amirante Arc, western Indian Ocean. *Earth Planet Sci Lett* 61, 127–135. [https://doi.org/10.1016/0012-821X\(82\)90045-0](https://doi.org/10.1016/0012-821X(82)90045-0)

Mishin, Y.A., Gerya, T. V., Burg, J.P., Connolly, J.A.D., 2008. Dynamics of double subduction: Numerical modeling. *Physics of the Earth and Planetary Interiors* 171, 280–295. <https://doi.org/10.1016/J.PEPI.2008.06.012>

Molnar, P., Stock, J.M., 2009. Slowing of India’s convergence with Eurasia since 20 Ma and its implications for Tibetan mantle dynamics. *Tectonics*. <https://doi.org/10.1029/2008TC002271>

Peral, M., Király, Á., Zlotnik, S., Funicello, F., Fernández, M., Faccenna, C., Vergés, J., 2018. Opposite Subduction Polarity in Adjacent Plate Segments. *Tectonics* 37, 3285–3302. <https://doi.org/10.1029/2017TC004896>

Peron-Pinvidic, G., Gernigon, L., Gaina, C., Ball, P., 2012. Insights from the Jan Mayen system in the Norwegian–Greenland sea—I. Mapping of a microcontinent. *Geophys J Int* 191, 385–412. <https://doi.org/10.1111/J.1365-246X.2012.05639.X>

Pusok, A.E., Stegman, D.R., 2020. The convergence history of India-Eurasia records multiple subduction dynamics processes. *Sci Adv* 6. [https://doi.org/10.1126/SCIADV.AAZ8681/SUPPL\\_FILE/AAZ8681\\_SM.PDF](https://doi.org/10.1126/SCIADV.AAZ8681/SUPPL_FILE/AAZ8681_SM.PDF)

Pusok, A.E., Stegman, D.R., 2019. Formation and Stability of Same-Dip Double Subduction Systems. *J Geophys Res Solid Earth* 124, 7387–7412. <https://doi.org/10.1029/2018JB017027>

Sandiford, D., Moresi, L., 2019. Improving subduction interface implementation in dynamic numerical models. *Solid Earth*. <https://doi.org/10.5194/se-10-969-2019>

Sengupta, S., Ray, K.K., Acharyya, S.K., de Smeth, J.B., 1990. Nature of ophiolite occurrences along the eastern margin of the Indian plate and their tectonic significance. *Geology* 18, 439–442. [https://doi.org/10.1130/0091-7613\(1990\)018<0439:NOOOAT>2.3.CO;2](https://doi.org/10.1130/0091-7613(1990)018<0439:NOOOAT>2.3.CO;2)

Spiegelman, M., Katz, R.F., 2006. A semi-Lagrangian Crank-Nicolson algorithm for the numerical solution of advection-diffusion problems. *Geochemistry, Geophysics, Geosystems* 7. <https://doi.org/10.1029/2005GC001073>

Stern, R.J., 2004. Subduction initiation: spontaneous and induced. *Earth Planet Sci Lett* 226, 275–292. <https://doi.org/10.1016/J.EPSL.2004.08.007>

Stern, R.J., 2002. SUBDUCTION ZONES. *Reviews of Geophysics* 40, 3–1. <https://doi.org/10.1029/2001RG000108>

Stevens, D.E., McNeill, L.C., Henstock, T.J., Delescluse, M., Chamot-Rooke, N., Bull, J.M., 2020. A complete structural model and kinematic history for distributed deformation in the Wharton Basin. *Earth Planet Sci Lett* 538, 116218. <https://doi.org/10.1016/J.EPSL.2020.116218>

Tilling, R.I., 1996. Hazards and Climatic Impact of Subduction-Zone Volcanism: A Global and Historical Perspective. *Geophysical Monograph Series* 96, 331–335. <https://doi.org/10.1029/GM096P0331>

1  
2  
3  
4  
5  
6  
7  
8  
9  
10  
11  
12  
13  
14  
15  
16  
17  
18  
19  
20  
21  
22  
23  
24  
25  
26  
27  
28  
29  
30  
31  
32  
33  
34  
35  
36  
37  
38  
39  
40  
41  
42  
43  
44  
45  
46  
47  
48  
49  
50  
51  
52  
53  
54  
55  
56  
57  
58  
59  
60  
61  
62  
63  
64  
65

845 Van Der Voo, R., Spakman, W., Bijwaard, H., 1999. Tethyan subducted slabs under India. *Earth*  
846 *Planet Sci Lett* 171, 7–20. [https://doi.org/10.1016/S0012-821X\(99\)00131-4](https://doi.org/10.1016/S0012-821X(99)00131-4)

847 Van Hinsbergen, D.J.J., Kapp, Paul, Dupont-Nivet, Guillaume, Lippert, Peter C, Decelles, Peter  
848 G, Torsvik, Trond H, Hinsbergen, V., Kapp, P, Dupont-Nivet, G, Lippert, P C, Decelles, P G,  
849 Torsvik, T H, 2011. Restoration of Cenozoic deformation in Asia and the size of Greater  
850 India. *Tectonics* 30, 5003. <https://doi.org/10.1029/2011TC002908>

851 van Hunen, J., Allen, M.B., 2011. Continental collision and slab break-off: A comparison of 3-D  
852 numerical models with observations. *Earth Planet Sci Lett* 302, 27–37.  
853 <https://doi.org/10.1016/j.epsl.2010.11.035>

854 Vignaroli, G., Faccenna, C., Jolivet, L., Piromallo, C., Rossetti, F., 2008. Subduction polarity  
855 reversal at the junction between the Western Alps and the Northern Apennines, Italy.  
856 *Tectonophysics* 450, 34–50. <https://doi.org/10.1016/J.TECTO.2007.12.012>

857 Westerweel, J., Roperch, P., Licht, A., Dupont-Nivet, G., Win, Z., Poblete, F., Ruffet, G., Swe,  
858 H.H., Thi, M.K., Aung, D.W., 2019. Burma Terrane part of the Trans-Tethyan arc during  
859 collision with India according to palaeomagnetic data. *Nature Geoscience* 2019 12:10 12,  
860 863–868. <https://doi.org/10.1038/s41561-019-0443-2>

861 Yang, S., Liang, X., Jiang, M., Chen, L., He, Y., Mon, C.T., Hou, G., Thant, M., Sein, K., Wan,  
862 B., 2022. Slab remnants beneath the Myanmar terrane evidencing double subduction of the  
863 Neo-Tethyan Ocean. *Sci Adv* 8, 1027.  
864 [https://doi.org/10.1126/SCIADV.ABO1027/SUPPL\\_FILE/SCIADV.ABO1027\\_SM.PDF](https://doi.org/10.1126/SCIADV.ABO1027/SUPPL_FILE/SCIADV.ABO1027_SM.PDF)

865 Yin, A., Harrison, T.M., 2000. Geologic Evolution of the Himalayan-Tibetan Orogen.  
866 <https://doi.org/10.1146/annurev.earth.28.1.211> 28, 211–280.  
867 <https://doi.org/10.1146/ANNUREV.EARTH.28.1.211>

868 Zhang, Q., Guo, F., Zhao, L., Wu, Y., 2017. Geodynamics of divergent double subduction: 3-D  
869 numerical modeling of a Cenozoic example in the Molucca Sea region, Indonesia. *J*  
870 *Geophys Res Solid Earth* 122, 3977–3998. <https://doi.org/10.1002/2017JB013991>

871 Zhou, X., Li, Z.H., Gerya, T. V., Stern, R.J., Xu, Z., Zhang, J., 2018. Subduction initiation  
872 dynamics along a transform fault control trench curvature and ophiolite ages. *Geology* 46,  
873 607–610. <https://doi.org/10.1130/G40154.1>

874 Zhu, M., Yan, Z., Pastor-Galán, D., Chen, L., Miao, L., Zhang, F., Li, S., Yang, S., 2023. Do  
875 microcontinents nucleate subduction initiation? *Geology* 51, 668–672.  
876 <https://doi.org/10.1130/G51222.1/5849054/G51222.PDF>



**Citation on deposit:** Roy, A., Mandal, N., & Van Hunen, J. (2024). Dynamic evolution of competing same-dip double subduction: New perspectives of the Neo-Tethyan plate tectonics. *Earth and Planetary Science Letters*, 647, Article 119032.

<https://doi.org/10.1016/j.epsl.2024.119032>

**For final citation and metadata, visit Durham Research Online URL:**

<https://durham-repository.worktribe.com/output/3106497>

**Copyright statement:** This accepted manuscript is licensed under the Creative Commons Attribution 4.0 licence.

<https://creativecommons.org/licenses/by/4.0/>